POLITECNICO DI TORINO

Master's Degree in Mechatronic Engineering

Master's Degree Thesis

Improvement of Energy Management Strategy of a Hybrid Electric Vehicle considering battery thermal behavior and State of Health

Supervisors

Prof. Andrea TONOLI

Dr. Stefano FAVELLI

Dr. Eugenio TRAMACERE

Eng. Andrea DELMASTRO

Candidate

Daniela D'ONOFRIO

December 2023

Summary

In the recent years there has been an increasing investment by car manufacturers in the production of electric and hybrid electric vehicles. The reason for this sudden change can be associated with the stringent environmental constraints imposed by government regulations. The consequence is that many researches are now focusing on the employment of new strategies to keep up with these restrictions. These studies develop technologies both at vehicle-level (control strategies) and subsystem-level (powertrain and energy storage components).
An important component to manage the power supply of Electric Vehicles (EVs) and Hybrid Electric Vehicles (HEVs) is the Energy Storage System (ESS). Batteries are the most common ESS component thanks to their energy density, compact size and reliability. When the vehicle undergoes significant variation of power, the battery cell, as the only element of ESS, may not be able to supply the required power demand or absorb the power from regenerative braking. To solve this problem, hybrid energy storage systems (HESS) combine two or more types of storage components with complementary features. One of the most functional combinations studied for a HESS is composed by supercapacitor and battery. Research results have proven that the use of supercapacitors in parallel with batteries greatly improves energy storage capabilities.
The vehicle considered in this thesis work is a 48V P1 hybrid light-duty commercial vehicle. This type of architecture leads to a high current rate due to the 48V. The solutions can be the limitation of the current, the employment of components with higher performance or adding a supercapacitor. In this work two different approaches are analyzed.

The first one considers the feasibility of a HESS composed by a supercapacitor in parallel of the main battery, while the second one considers the improvement of the EMS considering battery thermal behavior and State-of-Health estimation. Starting from the forward vehicle model in Matlab Simulink, the model of the supercapacitor is introduced and its performance analyzed. Then, a new battery model is introduced considering the thermal dynamics and cooling, while State-of-Charge and State-of-Health estimation algorithms are implemented.
The results of the analysis are twofold: on one hand, the introduction of the supercapacitor does not contribute to the improvement of the efficiency of ESS for the 48V P1 architecture. On the other hand, the thermal modeling and the algorithm to estimate the State-of-Health enhance battery usage if considered during the design of the EMS.

Acknowledgements

Desidero dedicare brevemente questo lavoro a tutte le persone straordinarie che sono state al mio fianco durante il mio percorso accademico. Il vostro sostegno e la vostra vicinanza hanno reso possibile questo importante traguardo. Grazie di cuore a ciascuno di voi.
Il mio primo pensiero va ai miei genitori. A mia madre, che è stata al mio fianco in ogni fase di questi 5 anni, dandomi la forza di andare avanti anche nei periodi più bui. Senza di lei, non ce l'avrei fatta. A mio padre, che, seppur lontano, ha saputo sdrammatizzare ogni mia ansia con il suo umorismo più unico che raro. Sei la persona più buona che io conosca, il mio eroe.
A mia sorella, che è sempre stata un faro nella mia vita, la mia ancora.
A Marco, che mi ha sempre dato ottimi consigli, come un buon fratello maggiore.
Ai miei nonni, il mio punto di riferimento. Questa tesi è dedicata soprattutto a voi, che mi avete spronato e avete sempre creduto in me, anche se tutt'ora non sapete cosa faccia un ingegnere meccatronico.
Ai miei zii, che sono come dei secondi genitori per me.
A Domenico, con il quale sono cresciuta insieme e so che sarà sempre ad un millimetro di cuore da me.
A Luca, piccolino di casa che piccolino non lo è più, spero tu sia fiero della tua cuginetta.
Un ringraziamento speciale va a Paolo, il mio sostenitore numero 1, orgoglioso di me in tutto ciò che faccio, colui che mi ha fatto sentire amata, che è stato sempre al mio fianco attraverso tutti gli alti e bassi. La tua gentilezza, il tuo sostegno e il tuo amore sono il mio tesoro più grande.

A Nadia, non una semplice amica ma una vera e propria complice. Sei stata presente dal giorno zero. Non ci sono parole per spiegarti quanto io sia grata di averti conosciuto quel pomeriggio del 1 Ottobre 2018 davanti all'aula 8. Sei stata il mio Virgilio, che mi ha accompagnato in questi 5 anni all'inferno. Con te ho condiviso tutte le tappe di questo percorso, in ogni risata e in ogni lacrima, tu c'eri. Sei la mia costante in questa esistenza altalenante.

Poi vorrei ringraziare le mie amiche di una vita. Siamo cresciute insieme, abbiamo preso strade diverse e ognuna di noi si sta realizzando in parti diverse d'Italia, ma nonostante tutto, io so che posso sempre contare su di voi. Soprattutto nell'ultimo anno, mi avete aiutato a prendere la vita con più leggerezza e mi avete fatto capire che la vera amicizia va oltre ai chilometri che ci dividono.

Ai miei "nuovi" amici, compagni conosciuti in questo mio percorso universitario che sicuramente porterò sempre nel cuore.

Vorrei dedicare questo lavoro a chi, purtroppo, non potrà mai festeggiare una festa di laurea, a chi non potrà mai scoraggiarsi per un esame andato male o che non si potrà mai realizzare nella vita perché la vita gli è stata tolta troppo presto. Ai miei tre angeli che mi hanno sempre dato forza.

E infine, vorrei esprimere la mia gratitudine al mio relatore, il Prof. Andrea Tonoli, che mi ha dato la possibilità di partecipare a questo progetto, a Stefano e Eugenio, che hanno reso possibile questo lavoro essendo presenti ogni volta in cui ne avevo bisogno. Senza la vostra guida, tutto questo non sarebbe stato possibile.

Table of Contents

List of Tables

List of Figures

Acronyms

CD
Charge Depleting

CS
Charge Sustaining

DoH
Degree of Hybridization

DP
Dynamic Programming

ECMS
Equivalent Consumption Minimization Strategy

EDL
Electric Double Layer

EECM
Equivalent Electric Circuit Model

EKF
Extended Kalman Filter

EM
Electric Motor

EMS

Energy Management System

ESR

Equivalent Series Resistance

ESS

Energy Storage System

FLC

Fuzzy Logic Control

GRV

Gaussian random variable

GVT

Global Vehicle Target

HESS

Hybrid Energy Storage System

HEV

Hybrid Electric Vehicle

ICE

Internal Combustion Engine

MPC

Model Predictive Control

OCV

Open Circuit Voltage

SC

Supercapacitor

SOC

State Of Charge

SOH

State of Health

UC

Ultracapacitor

UT

Unscented Transformation

Chapter 1

Introduction

1.1 Background

The automotive sector significantly contributes to global pollution. According to the European Environment Agency's report, the transportation sector accounted for nearly 25% of the total greenhouse gas emissions in the European Union in 2019, with road transportation contributing to 72% of this figure [1]. Greenhouse gases, including CO_2 and NO_x, have adverse effects not only on climate change (due to the greenhouse effect contributing to the rise in global temperatures) but also on human health, leading to respiratory diseases.
As a result, the reduction of vehicle emissions has become a crucial focus for both governments and the automotive industry. The European Union aims to achieve a 90% reduction in greenhouse gas emissions from transportation compared to 1990 levels by the year 2050.

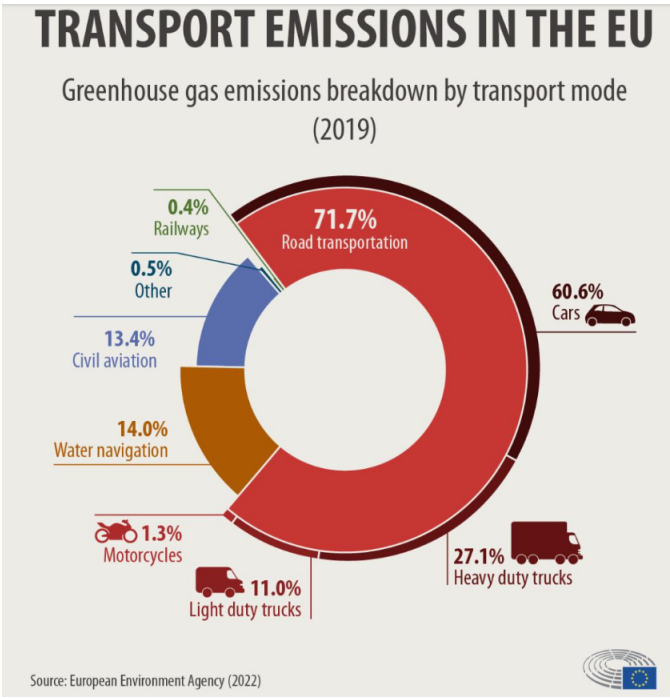

Figure 1.1: Transport emission in UE [2]

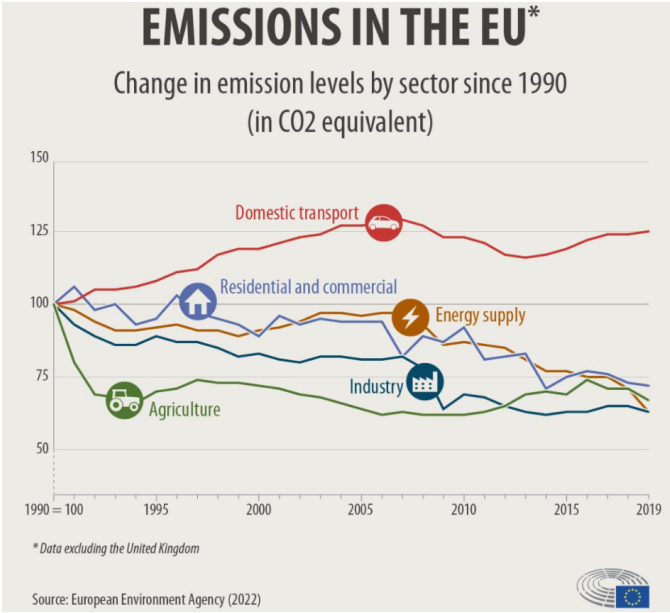

Figure 1.2: Evolution of CO2 emissions in the EU for each sector (1990-2019) [2]

1.1.1 Electrification

Electrification plays a significant role in reducing vehicle emissions. Electrification involves replacing thermal power (obtained from fuel) with electric power, a shift that can manifest in the form of pure electric vehicles or hybrid electric vehicles that retain a combustion engine.

According to the European Environment Agency's report on "Electric vehicles from life cycle and circular economy perspectives" [3], the greenhouse gas emissions over the entire life cycle of electric vehicles are up to 30% lower compared to petrol and diesel cars. With the ongoing decarbonization of the EU's energy mix, this percentage is anticipated to reach 73% by 2050 [4].
The electric car market has experienced significant growth in sales, increasing from 4% of total car sales in 2020 to 14% in 2022. This surge is attributed not only to government incentives for electric vehicle purchases but also to the continually rising fuel costs. Additionally, electric vehicles contribute to a reduction in noise pollution, further enhancing environmental quality.

1.2 Project overview

This thesis is a component of the "AutoEco" project, funded by Pi.Te.F. (Piattaforma Tecnologica di Filiera) in the Piedmont region, in collaboration with Politecnico di Torino, Dayco Europe S.r.l, Podium Advanced Technologies, and other companies. The primary objective of this project is the hybridization and automation of a light-duty hybrid electric vehicle, with the goal of reducing fuel consumption and enhancing energy efficiency.

1.3 Thesis outline

This thesis comprises four chapters:

1. The initial chapter (Introduction) provides a project overview, a

brief introduction to electrification a summary of transport CO_2 emissions produced in the EU in past years until today.

2. The second chapter (Theoretical Background) presents a comprehensive exploration of hybrid vehicles and associated technologies. It includes a detailed categorization of hybrid electric vehicles, accompanied by explanations of various energy management control strategies and energy storage systems. The chapter also introduces a description of the characteristics of supercapacitors and batteries focusing on the depiction of the various types of the latter.

3. The third chapter (Methodology), includes a vehicle model overview centering on energy analysis of it. Furthermore, it encompasses batteries and supercapacitors modeling. The chapter also contains the description of battery thermal dependence including the description of the Matlab model used in this thesis work. The last part of this chapter includes the explanation of the Kalman filter used to calculate the estimate of the State-of-Charge and State-of-Health to improve the previously used model with the addition of these estimators.

4. The fourth chapter (Simulation and Results) compiles all the findings, elucidated through the utilization of figures and tables.

5. The final chapter is devoted to the conclusion, succinctly restating the key aspects of the project and offering insights into potential future developments.

Chapter 2

Theoretical background

2.1 Hybrid Electric Vehicle

Hybrid Electric Vehicle (HEV) provides an alternative source of energy for vehicle propulsion by integrating electric motors with an internal combustion engine. A battery integrates the power of the internal combustion engine (ICE) and allows it to operate in a more efficient region, thus improving fuel economy. Other advantages that HEVs can offer are the reduction of carbon and toxic gas emissions and the improvement of powertrain performance since the electric system assists the engine in functioning in its efficient range.

2.2 HEVs Classification

HEVs are usually classified according to three parameters:

1. Degree of hybridization

2. Electric motor position

3. Powertrain architectures

2.2.1 HEVs classification based on hybridization

The most important classification made on hybrid vehicles is related to the degree of hybridization; generally, four different degrees of hybridization can be defined

- **Micro hybrid**: It is the lightest form of hybridization. The original system comes with a small electric machine which has the function of replacing the starter motor and the alternator. So, in this type of system, the necessary energy is provided by itself thermal engine and, for this reason, we are not talking about true hybrid systems.

- **Mild hybrid**: It is the most used form of hybridization today. This system typically only provides a boost to the ICE and, for this reason, it is unable to propel the vehicle on electric power alone. The electric motor can be used also for braking, in this way, part of the kinetic energy can be converted into electric energy to charge the battery.

- **Full hybrid**: This type of vehicle is capable of driving in pure electric mode but only for a short distance, depending on battery capacity. Therefore, in a full hybrid vehicle, there are three operation modes: engine only, battery only, and a combination of both.

- **Plug-in hybrid**: The most powerful powertrain is contained in this type of HEV. Unlike the full hybrid, with the plug-in hybrid we can travel longer distances in pure electric. This is made possible thanks to more powerful batteries which are recharged through the electrical grid.

Type of hybrid	Battery Voltage [V]	Electric machine power [kW]	Pure electric mode range [Km]	CO_2 estimated reduction benefit [%]
Micro Hybrid	12	2-3	0	5-6
Mild Hybrid	48-160	10-15	0	7-12
Full Hybrid	200-300	30-50	5-10	15-20
Plug-in Hybrid	300-400	60-80	<100	>20

Table 2.1: Characteristics of various hybrid electric vehicles

2.2.2 HEV's classification based on position of electric motor

Another possible classification is based on the position of the electric motor with respect to the ICE. As it is shown in Figure 2.1, we can have different types of hybrid configurations.

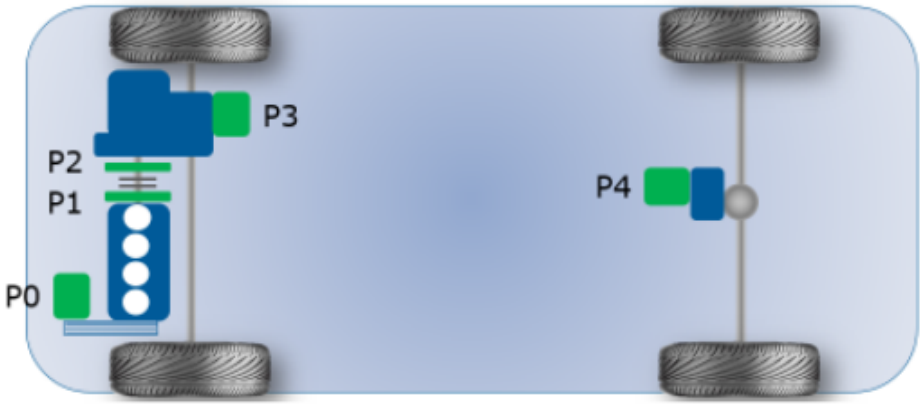

Figure 2.1: HEVs classification based on EM position

- **P0**: The electric machine is connected directly via the belt system to the engine. The advantage of this configuration is the low cost.

The disadvantages are the impossibility of mechanical disconnection between the electric machine and ICE and the limitation of power and torque due to the restricted space for the installation.

- **P1**: The electric machine is placed in the crankshaft of the engine, just like in P0, it is connected directly. For this reason, in this configuration, the electrical machine and ICE work together. The differences between P0 and P1 configurations are that in the latest can provide higher torque and a more efficient regenerative braking.
- **P2**: The electric machine is connected to the input shaft of the transmission. On the contrary of the previous configurations, in P2 architecture the electric machine and ICE can be mechanically disconnected by using a clutch or a set of clutches.
- **P3**: The electric machine is mounted at the output shaft of the transmission. Since between the wheels and the electric car, there is only the differential, a maximization of regenerative braking is obtained. Another advantage of this configuration is the increase in torque, so there is the opportunity to choose the speed of the two motors separately.
- **P4**: The electric machine is placed on the rear axle drive. This is the most optimized configuration. Furthermore, P4 architecture allows the four-wheel drive if the ICE is connected to the front axle drive.

2.2.3 HEVs classification based on powertrain layout

The last classification is based on powertrain architecture. All the architecture discussed in subsection 2.2.2 are considered parallel hybrid but the powertrain can be classified also as series hybrid and series/parallel hybrid.

- **Parallel hybrid**: The ICE and the electric motor are directly mechanically connected using a joint. Power from ICE and from

electric motor are summed together therefore a clutch is needed. When the clutch is disengaged, the vehicle can be pushed using only the battery, allowing pure electric mode. When the clutch is engaged it is possible to obtain different operating modes: ICE only, the two energy sources can simultaneously provide power to the transmission and ICE can be used to charge the battery during regenerative braking events.

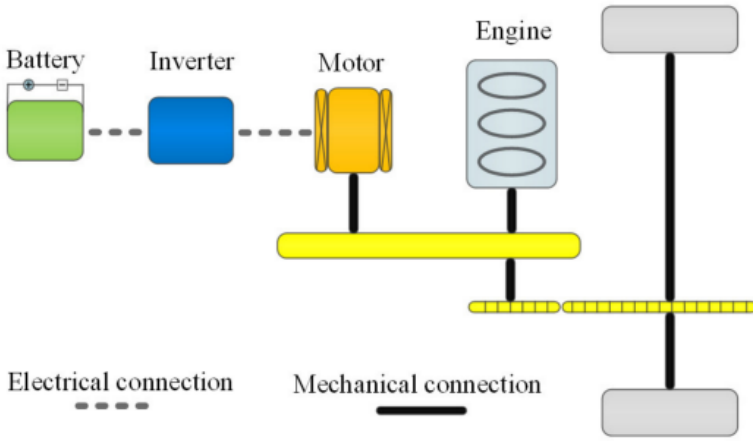

Figure 2.2: Parallel Hybrid architecture [5]

- **Series hybrid**: The two sources of energy are in series. More precisely, the ICE gives mechanical energy to the generator which produces electrical energy to be given as input to the electric motor. The latest converts the electric energy into mechanical one to drive the wheels. This type of mechanism causes the presence of many losses.

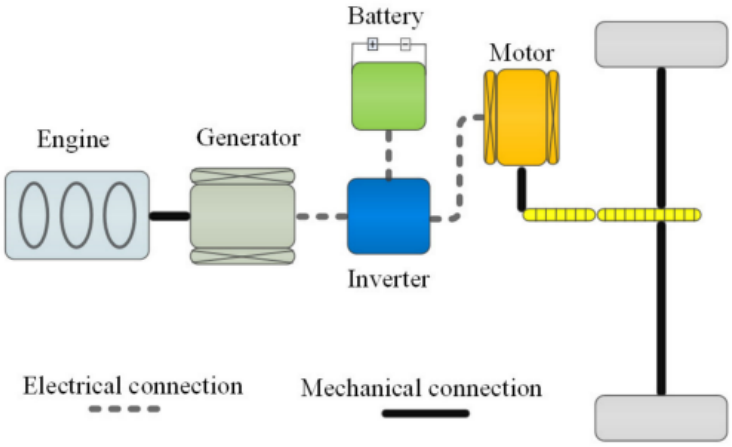

Figure 2.3: Series Hybrid architecture [5]

- **Series/parallel hybrid**: This is the most flexible architecture. This configuration offers the advantages of both series and parallel architecture thanks to a power slit device which is used to switch between different operating modes.

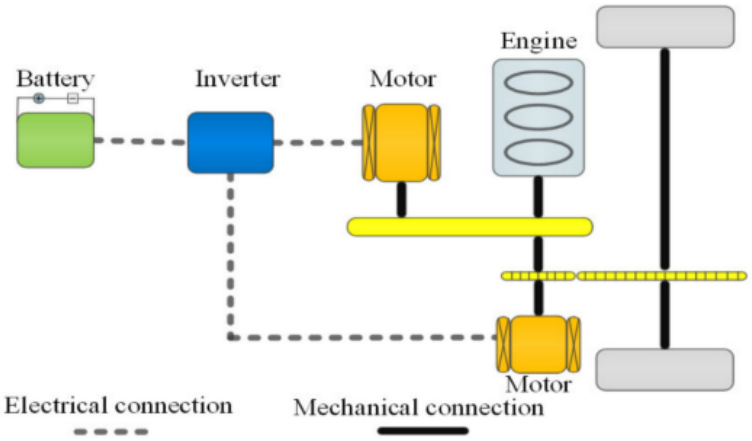

Figure 2.4: Series/parallel Hybrid architecture [5]

2.3 HEVs operating mode

HEVs can have different operating modes:

1. **ICE only**
   All the power is given by the internal combustion engine.

2. **Hybrid mode**
   The power required is given simultaneously by the internal combustion engine and the electric motor.

3. **Engine drive and battery charging**
   Only the internal combustion engine gives the required torque to the wheel. If the engine produces more power than the one required and the battery SOC is low, some of this power is given to the battery for its recharge.

4. **Engine and motor drive and battery charging**
   Both engine and electric motor give the power requested. As in the previous operating mode, a part of ICE's power is used to charge the battery.

5. **Regenerative braking**
   During the braking action, the electric motor becomes a generator by converting the kinetic energy, that would be wasted, into electrical energy useful for charging the battery.

6. **Electric motor only**
   All the power is given by the electric motor.

2.4 Energy Storage Systems (ESS)

One of the most important components of Electric Vehicles (EVs) and Hybrid Electric Vehicle (HEVs) is the Energy Storage System (ESS). Commonly, ESS can be classified into two categories:

1. High-frequency components such as a sudden increase in energy demand

2. Low-frequency components such as renewable energies or daily energy consumption resources

Batteries are the most common energy storage component for EVs and HEVs thanks to their energy density, compact size, and reliability. However, as it is shown in the table below, the battery cell has low specific power.

Energy storage system	Energy density	Power density	cycle life	response time	Cost
chemical battery	high	low	short	medium	low
sodium-sulphur battery	medium	low	short	slow	medium
flywheel	low	high	long	fast	high
supercapacitor	low	high	long	fast	medium
superconducting magnetic	medium	high	long	fast	high

Table 2.2: Characteristics of different ESS element [6]

These elements, taken individually, none of them respond optimally to both high and low-frequency power exchanges, furthermore, in EV/HEV when the vehicle undergoes a significant variation of power, the battery cell, as the only element of ESS, may not be able to supply the required power demand or absorb the power from regenerative braking. Even if the power demand is supplied or the available regenerative braking power is absorbed, due to the huge fluctuations of charge/discharge current, the efficiency and consequently, the lifetime of the battery cells are compromised [7]. To solve this problem, hybrid energy storage systems (HESS) combine two or more types of storage components with complementary features.

2.4.1 Hybrid Energy Storage Systems (HESS)

A Hybrid Energy Storage System (HESS) is a combination of different energy storage technologies designed to work together to optimize energy management and provide a more reliable and efficient energy supply. It typically combines two or more types of energy storage systems, such as batteries, ultracapacitors (supercapacitors), flywheels, and more, to address various energy storage requirements in a unified manner.
One of the most functional systems studied in recent years is the HESSs composed of batteries and Ultracapacitors (UCs) due to their capacity being much bigger than conventional ones and their high specific power levels. The combination of such different systems allows the EVs/HEVs to operate during extended driving range because the battery can ensure only the average power and the supercapacitors can ensure the power variation. Therefore, UCs are usually used to absorb the high power of regenerative braking and supply maximum power for acceleration, whereas the batteries are used for vehicle operations involving less power [8].
As well as being applied to hybrid vehicles, HESS is often used in applications like renewable energy integration, microgrids, and industrial settings where maintaining a stable power supply and managing fluctuations in energy demand are critical. It allows for a versatile and adaptable approach to energy storage, meeting the specific needs of different applications. The chart below compares the energy density of fuel cells, batteries, ultracapacitors, and conventional capacitors versus their specific power.
From figure 2.5 it is clear why we choose to combine battery and UCs to realize the required energy and power characteristics.

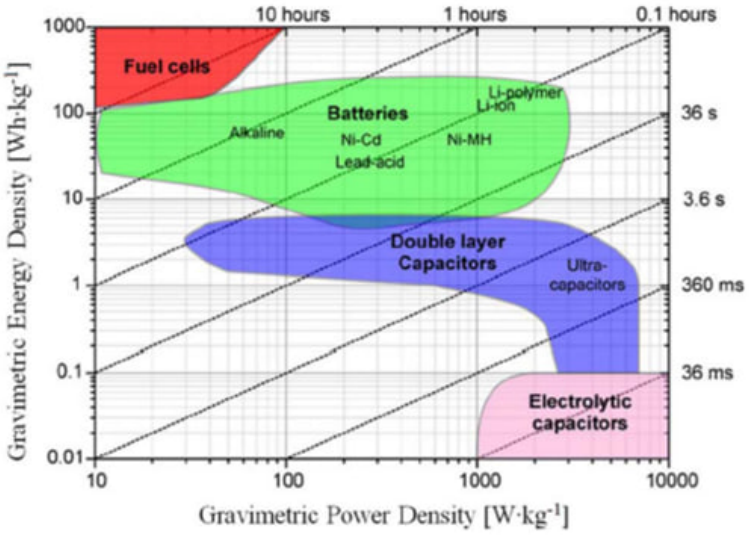

Figure 2.5: Ragone curve[7]

The advantages of a Hybrid Energy Storage System include:

1. Improved Energy Management: HESS balances power and energy requirements allowing for better control of energy sources. In fact, with this type of technology, it is possible to store excess energy during periods of low demand and release it during peaks in demand.

2. Enhanced Energy Efficiency: Combining different types of energy storage together can provide greater overall efficiency and faster response to load changes.

3. Increased Reliability: If one component fails or reaches the end of its life cycle, the others can continue to provide energy.

4. Extended Lifespan: Combining different energy storage helps to reduce the stress of by potentially extending the overall lifetime of the system.

5. Rapid Power Delivery: Some energy storage technologies, like ultracapacitors, excel at delivering power quickly, making them suitable for applications where rapid power output is essential.

In [9] is analyzed the differences between Battery Energy Storage (BESS) and HESS show that BESS has higher efficiency in electricity cost and less capital cost than HESS. The HESS benefit is obtained by increasing the time between replacements of the battery pack. For BESS, the battery pack will be replaced twice during the 10 years, which will significantly increase the cost. Based on current prices the total cost of HESS, including capital cost, electricity cost, and battery replacement cost, is 25.9 % less than that of BESS.

2.4.2 HESS typologies

In literature, different HESS topologies have been studied in which various architectures using batteries and supercapacitors have been proposed. In general, battery-supercapacitor can be categorized based on their connection topology as depicted below:

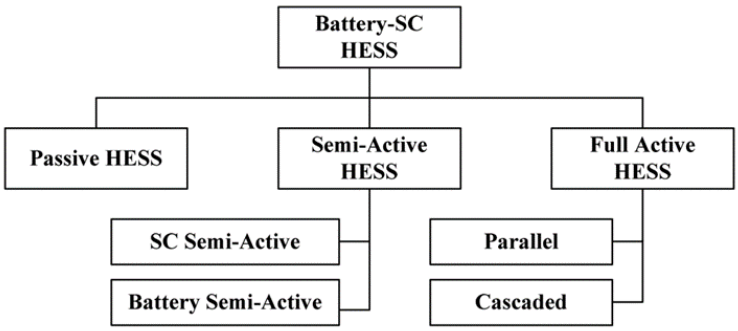

Figure 2.6: Classification of battery-SC HESS typologies [6]

Passive connection is the simplest and cheapest HESS topology in which the battery and UCs are connected to the DC bus directly, hence, they share the same terminal voltage. In the semi-active connections power electronic converters are situated between the battery or UCs and the DC bus, which means that only one of the two ESS components is actively controlled. On the other hand, in the fully active components both the battery and supercapacitor are both actively controlled by bidirectional DC/DC converters. We can make a further subdivision within the following categories:

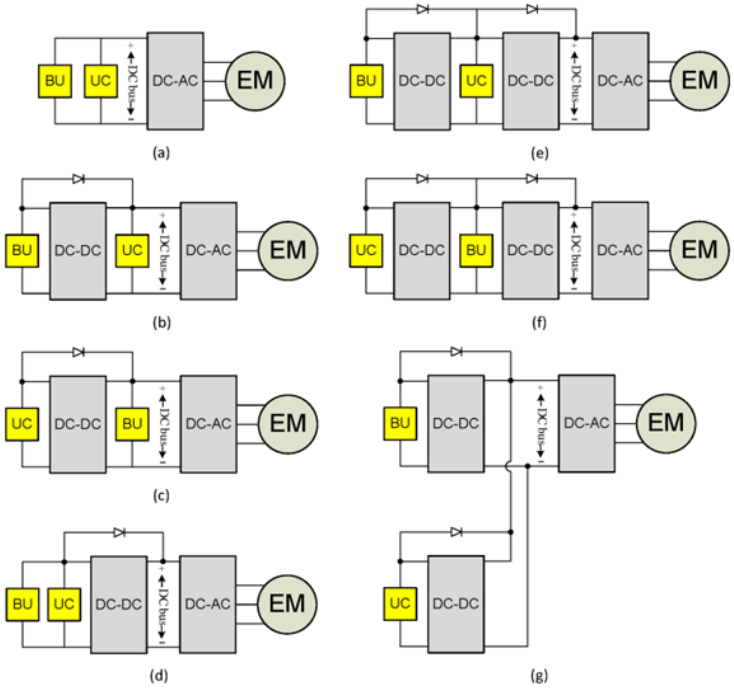

Figure 2.7: Different architecture of battery-SC [7]

Figure 2.7(a) shows a direct connection of the Battery unit and UC to the DC bus hence a passive connection. Given that the control system is simple, this configuration is easy to build and cheaper. However, since the BU is directly to the DC bus, it can be exposed to large and fast variations of discharge/charge currents, causing the deterioration of the battery with a reduction of battery life. Two typologies exist for the semi-active configuration: the one in Figure 2.7(b) where UC is connected directly to the DC bus and the other one in Figure 2.7(c) where the battery unit is directly connected to the DC bus. In the first typology, due to the fact that the battery is decoupled from the DC bus, it is possible to solve the problem that is shown in the configuration in Figure 2.7(a), in fact, the power demand is picked up by the UC at the DC bus and battery can be controlled. The only problem with this configuration is that now the DC bus voltage may be exposed to large and fast variations. In the second topology DC bus does not undergo significant voltage variations as in the first one but the battery

is exposed to high charge/discharge fluctuations. One of the good things about this topology is that UC can operate over a wide voltage range. For the full active configuration, we can distinguish two main typologies: Cascade and Parallel. The simplest one is shown in Figure 2.7(d) where the battery and UC are parallel-connected, and they are decoupled from the DC bus by a DC-DC converter. Although there are some controls over the output power of battery-UC, it still suffers from limitations of UC as it is clamped to the battery. Cascade typologies are shown in Figures 2.7(e) and 2.7(f) where the main difference between these two configurations is the position of the battery unit and UC, they are reversed. In the configuration in Figure 2.7(e) the battery is connected to the lowest voltage terminal and the UC is installed at the intermediate voltage level. In this way, the UC voltage is free to fluctuate, and this is a big problem for the stability of the system. A solution for this problem could be to swap the positions of the battery and UC, as shown in Figure 2.7(f). In this way, the battery is more stable, but cell balancing could be difficult to manage at high voltage. A crucial drawback of the cascaded typologies is the potential stability problems as they can represent a DC-DC converter. The last configuration in Figure 2.7(g) is a parallel-converter typology. All the stability problems are solved in this configuration by classifying converters for battery and UC separately.

2.4.3 Power converters

From the previously explained architectures, we can see that another fundamental element for HESS technology is present. A DC-DC converter is an essential component found on an HEV powertrain, with unidirectional and bidirectional variants existing. Bidirectional converters have two modes of operation: The first is boost, also known as a step-up converter, it takes an input voltage that is typically lower than the desired output voltage and raises it to a higher level, while the second is called the buck, also known as a step-down converter, it takes an input voltage that is typically higher than the desired output voltage

and decreases it to a lower level (used for battery charging). The typology of the converter can be further divided into isolated or non-isolated. The main task of the converter is to control the energy flows between the battery and the supercapacitor and to transport energy to the load. Therefore, the insertion of the converter safeguards the system and protects the battery from load energy peaks, thus increasing its life. Every phase of the power converter became crucial because you have to choose the typology, the operating mode, the switching frequency and make thermal consideration for safety.
The most famous HESS architecture is the one with a battery and supercapacitor in parallel. The main problem of this configuration is that the power shared between the battery and supercapacitor is determined by their respective series resistances. The consequence is that the output voltage follows the battery charge/discharge curve. Placed a converter between the two ESS to avoid this phenomenon. Research demonstrates that the total losses of a HESS system with a DC/DC converter can be reduced by a third compared to the losses of a HESS system consisting only of batteries and supercapacitors of the same size. Unfortunately, adding a DC/DC converter increases the cost and weight of the entire system. Since the converter must work at a high switching frequency in order to reduce the weight and dimensions of the magnetic elements present in the converter itself and since it is not easy to satisfy all the requests with traditional Buck and Boost converter, in [10] is modeled a type of converter that solve these problems. This DC/DC converter has four operating modes:

- Buck mode for acceleration
- Boost mode for acceleration
- Buck mode for braking
- Boost mode for braking

In order to realize all four possible modes of operation they chose to adopt a scheme of four bridge valves.

2.5 Supercapacitors

Supercapacitors are particular types of capacitors that are able to store a large quantity of charge (1000 Farad). They have specific power and energy bigger than the traditional capacitors. In fact, as shown in Table 2.2, supercapacitors have important features such as high-power density, long lifetime, fast charging capabilities, and environmental safety with no gas emissions that made them popular in applications like electric and hybrid vehicles, wireless sensor networks, memory backup system, power bank for improvement of battery performances. However, supercapacitor has some disadvantages like less energy density and higher self-discharge at no load condition, the latter becomes a serious issue when the long-term response of a supercapacitor is important. The reason behind the self-discharge is the redistribution of charge into the porous structured carbon electrode by diffusion and leakage current flow through the ohmic path between electrode-electrolyte interfaces [11].

2.5.1 Chemical Structure

As it is described in [12], SCs do not have dielectric material between positive and negative electrodes. Instead of an electrolyte that has positive ions and negative ions filled between the two electrodes, it uses the electrical double layer (EDL) that is formed at the interface of the solid electrode and liquid electrolyte. An electrical double layer is formed at each interface where the active carbon powder contacts the electrolyte as shown in figure 2.8. So, whenever a charged surface comes into contact with any electrolyte solution, a potential difference is created between the surface and the solution by attraction and repulsion of ions of opposite and equal charge, respectively. This layer of opposite charges is called an electrical double layer (EDL).

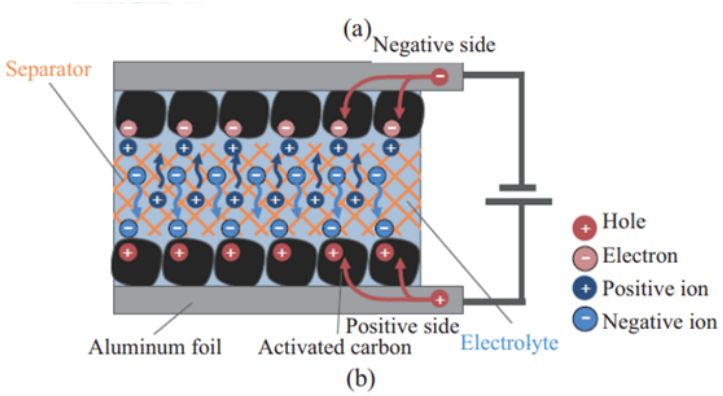

Figure 2.8: Structure of SCs [12]

The SCs are charged by ions moving through the carbon surface (figure 2.9) and discharged by reverse moving away of ions (figure 2.9). The capacitance value of SCs is dependent on the surface area.

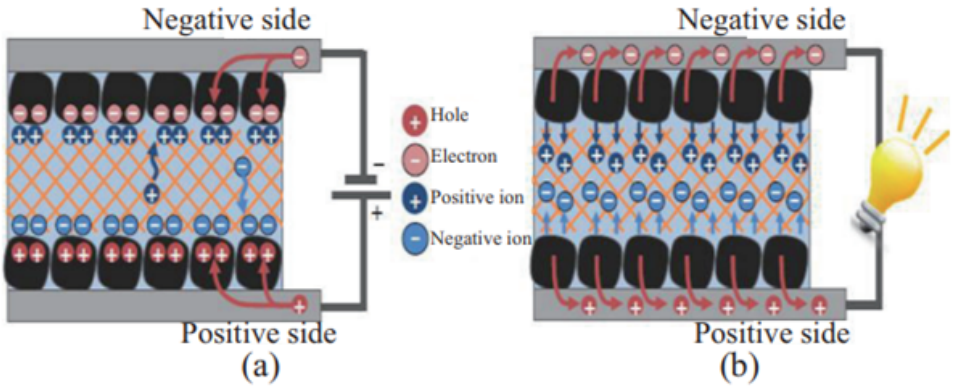

Figure 2.9: (a) Charge (b) Discharge [12]

The stored energy is higher than a classic capacitor because the charge separation occurs in the electrolytic double layer. Below the equations of a parallel capacitor:

$$C = \epsilon_0 \epsilon_r \frac{S}{d}$$

$$W = \frac{1}{2}CV^2$$

Where C is the capacity, ϵ_0 is the permittivity of free space (8.859 pF/m), ϵ_r is the relative permittivity, W is the stored energy, V is the voltage of the capacitor.

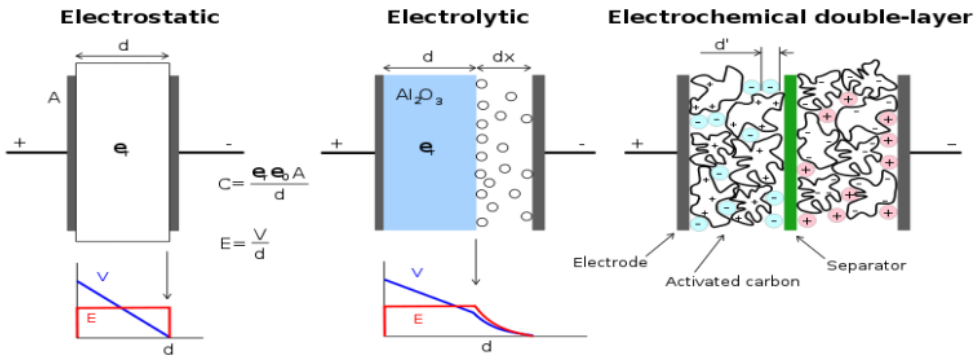

Figure 2.10: Comparison between capacitors and supercapacitors

However, in addition to the resulting capacity due to the high coal surface area, a contribution is obtained from the separation of charges obtained in the double-layer also from reactions that can occur on the surface of the coal. These reactions cause a further accumulation of electric energy that leads to a reduction of the supercapacitor's life cycle.
To conclude, the advantages and disadvantages of supercapacitors are briefly listed.

- **Advantages**
  - High power density
  - Long lifetime
  - Fast charging capability
  - Environmentally safe
  - Low internal resistance

  - High efficiency

- **Disadvantages**
  - Low energy density
  - High self-discharge at no load condition
  - Low voltages for single cells

2.6 Batteries

As described previously in paragraph 2.4, a battery is one of the most common energy storage systems due to its high energy density, low self-discharge rate, and no memory effect. In the aspect of technology, the rechargeable battery is improved from a lead acid battery to a nickel-based battery and from a nickel-based battery to a lithium-ion (Li-ion) battery. In this subsection, the main battery storage systems present on the market will be described.
Lead-acid batteries: Lead-acid batteries are the oldest rechargeable battery system. Although they are known for their robustness and low cost, they have a low energy density and a limited number of charging cycles.
Nickel-cadmium batteries: Nickel-cadmium (NiCd) is used in applications that require extended life, high discharge currents, and the ability to operate in extreme temperature environments. Despite their renowned robustness and resistance, NiCd batteries have the significant drawback of suffering from a marked memory effect.
Nickel-metal-hydride batteries: They are the perfect replacement for NiCd as the latter cause environmental problems due to the chemical products used. An advantage of this type of battery is the high specific energy.
Lithium-ion battery: They have higher terminal voltage, higher power density, and higher energy density compared to the other rechargeable batteries, moreover, Li-ion cells are now widely used in EV/HEV applications. In [13] it is explained that modern Li-ion batteries are composed of three parts soaked in electrolyte solution: two electrodes

and one separator which is a permeable membrane placed between the two electrodes to keep them apart to prevent electric short circuits. Usually, carbon material doped with lithium is used as the negative electrode, and a metal oxide material containing lithium as the positive electrode. During the discharge process of Li-ion batteries, the lithium active particles diffuse up to the surface of the negative electrode and react, then, the produced lithium ions flow through the electrolyte and arrive at the positive electrode where they react with the metal oxide material and diffuse into it. The electrons produced at the negative electrode cannot pass through the separator, so they flow through the external circuit, producing the current. The inverse reactions occur when charging the battery.

2.6.1 Types of lithium-ion batteries

Lithium-ion batteries are named after the acronyms of the active materials they are made from composed. For example, lithium and cobalt oxide, one of the most common Li-ion ions, have chemical symbols LiCoO2 and abbreviation LCO. Cobalt is the main active material that gives particular characteristics of the battery [14].

- $LithiumCobaltOxide(LiCoO_2)$: The battery is made of an oxide lithium-cobalt cathode and a lithiated graphite carbon anode. The drawback of Li-cobalt is its short lifespan, low thermal stability, and low specific power.

- $LithiumManganeseOxide(LiMn_2O_4)$: This battery has a mix of oxide manganese and lithium as cathode material. An added benefit of this structure is the high thermal stability and increased safety, however, the lifespan is limited.

- $LithiumNickelManganeseCobaltOxide(LiNiMnCoO_2oNMC)$: To improve specific energy and prolong Li-manganese battery lifespan, it mixes with lithium nickel manganese cobalt oxide (NMC). This cathode combination is one of the most successful Li-ion systems. Nickel is known for its high specific energy but poor stability, on the other hand, manganese has great stability but low

specific energy. The combination of the two metals allows them to compensate for the weak sides of each of them.

- $Lithium Nickel Cobalt Aluminum Oxide (LiNiCoAlO_2 o NCA)$: They are similar to NMC but with high energy specific. Furthermore, they have reasonably good specific power and long life.

- $Lithium Titanate (Li_4Ti_5O_{12})$: Li-titanate replaces the graphite in the anode of a typical lithium-ion battery. The cathode can be lithium manganese oxide or NMC. The advantage of titanate is that it is safe, has thermal stability at high and low temperatures, and is, therefore, better than other lithium-ion systems. However, the battery is expensive and has low specific energy.

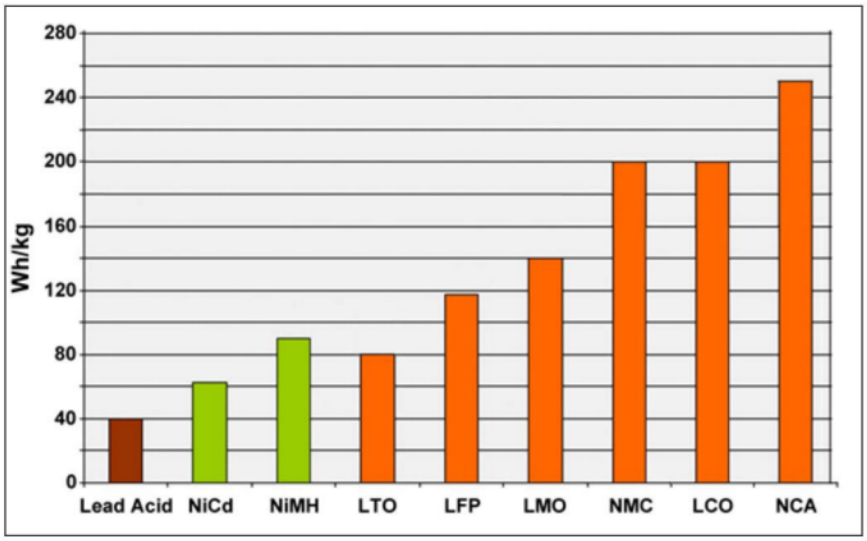

Figure 2.11: Specific energy in different BESS [14]

2.6.2 Battery characteristics

Accurate information about batteries, such as the state of charge (SOC), Open circuit voltage (OCV), and temperature, is essential for circuit designers to manage the energy consumption of battery-powered systems.

- The State of Charge (SOC) is a relative measure of the amount of energy stored in a battery, defined as the ratio between the amount of charge that can be extracted from the cell at a given moment and the total capacity.

$$SOC\% = 100\frac{(Q_0 + Q)}{Q_{max}}$$

  Where Q_0 is the internal charge of the battery, Q the electricity delivered by or supplied to the battery, Q_{max} is the total capacity.

- The Depth of Discharge (DOD) is the amount of charge that already dissipated from the battery.

$$DOD = 1 - SOC$$

- Open Circuit Voltage (OCV) is the battery terminal voltage when the battery's internal equilibrium is reached in the absence of load. Battery OCV depends on the SOC, temperature, and previous charging/discharging history, which is referred to as the hysteresis effect.

- Temperature influences the battery capacity, as explained in [15], battery rated capacity is usually measured at room temperature, e.g., $25°C$. The available capacity decreases as temperature decreases and can be halved when the temperature falls below $-20°C$. Temperature also has an influence on battery internal resistance. When the temperature inside a battery increases, the electrons are excited, therefore, the internal resistance will decrease, and the battery can produce a larger current. In EV/HEV applications, a thermal model that can predict battery temperature under various charging and discharging conditions is necessary for developing thermal management algorithms and cooling strategies.

- Aging condition can be indicated by two factors: capacity fading or internal resistance increment. Battery capacity fading is the permanent capacity loss after a certain period of storage or usage, and battery end-of-life is usually defined as when the capacity falls below 80% of its nominal capacity. There are two different types of battery aging processes, namely calendar life (capacity fading due to storage) and cycling (capacity fading due to usage).
- State of Health (SOH) characterizes the ability of the current battery to store energy relative to the new battery. It can be defined as:

$$SOH\% = 100\frac{C_{aged}}{C_{rated}}$$

Where C_{aged} is the current capacity of the battery, C_{rated} is the rated capacity of the battery.
The internal resistance R_0 is an important indicator of the aging of a battery. In fact, the SOH can be calculated also as follows:

$$SOH\% = 100\frac{R_{EOL} - R_0}{R_{EOL} - R_{new}}$$

Where R_{EOL} is the internal resistance at the end of life, R_0 is the internal resistance of the current battery, and R_{new} is the internal resistance of the new battery.

A summary representation of the three main statuses (SoC, SoH, and DoD) of the battery related to the capacity.

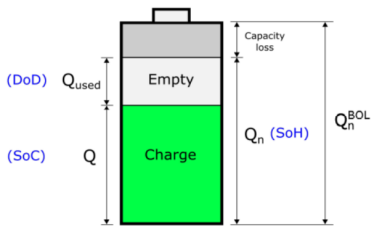

Figure 2.12: SoC, SoH, and DoD

Comparison between battery and supercapacitor

The table compares the parameters of the three main categories of supercapacitors with electrolytic capacitors and lithium-ion batteries.

Parameter	Aluminium electrolytic capacitors	Double-layer capacitors	supercapacitors for power applications	Pseudo/hybrid capacitors Li-ion cap	Li-ion batteries
Temperature range [$^{\circ}C$]	-40 to 125	-20 to 70	-20 to 70	-20 to 70	-20 to 60
Cell Voltage [V]	4 to 550	1.2 to 3.3	2.2 to 3.3	2.2 to 3.8	2.5 to 4.2
Charge/ Discharge Cycles	unlimited	10^5 to 10^6	10^5 to 10^6	$2 * 10^4$ to 10^5	500 to 10^4
Capacitance range [F]	< 1	0.1 to 470	100 to 12000	300 to 3300	-
Energy density [Wh/Kg]	0.01 to 0.3	1.5 to 3.9	4 to 9	10 to 15	100 to 265
Power density [kW/Kg]	> 100	2 to 10	3 to 10	3 to 14	0.3 to 1.5
self-discharge time at $25^{\circ}C$	days	weeks	weeks	month	month
Efficiency [%]	99	95	95	90	90
Lifetime at $25^{\circ}C$ [Years]	>20	5 to 10	5 to 10	5 to 10	3 to 5

2.7 Energy Management System (EMS)

The energy management system is a mechanism created to monitor, control, and optimize the performance of a system. The aim of the EMS in a HEV system is to determine the optimal power split between the on-board energy source. Deciding the amount of power delivered by the different energy sources of an HEV in such a way as to follow a certain driving path is the main problem faced by the EMS. The control of this type of vehicle is divided into two paths: Low-level control and High-level control. The low-level control manages the energy sources, it is responsible for providing the requested power and it is then performed on single components using traditional closed-loop control methods. On the other hand, high-level control is responsible for energy optimization on vehicles. Its task is to receive information about the amount of requested power from the driver and send this data to the actuator controllers. This type of control is the energy management system (EMS). The driver's desires are translated into actions by the low-level control.

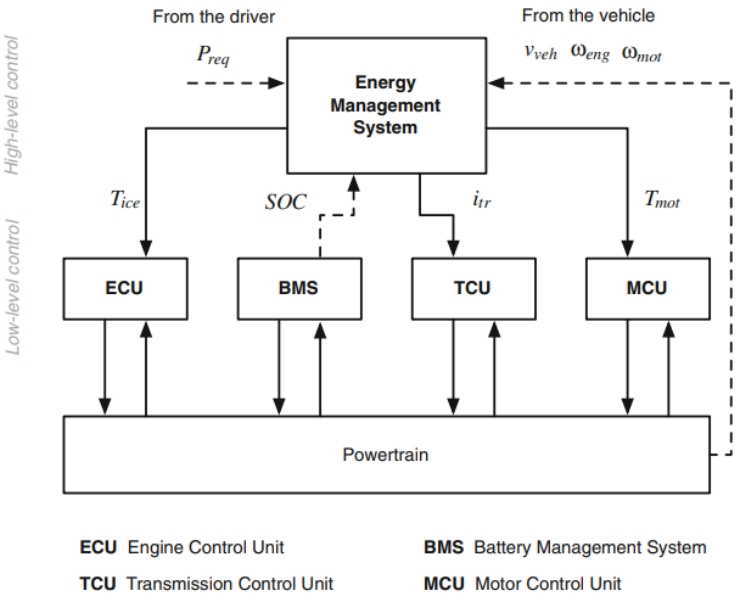

Figure 2.13: Energy Management System

So the purpose of the control strategy is to allocate the output/input power according to the characteristics of the two power sources as well as to improve the power efficiency and dynamic performance. Due to the complex and non-linear characteristics of vehicle components, a simple power allocation method may be not enough to allocate the power demand among the energy storage elements, for this reason, advanced supervisory control algorithms for EMS have been developed.

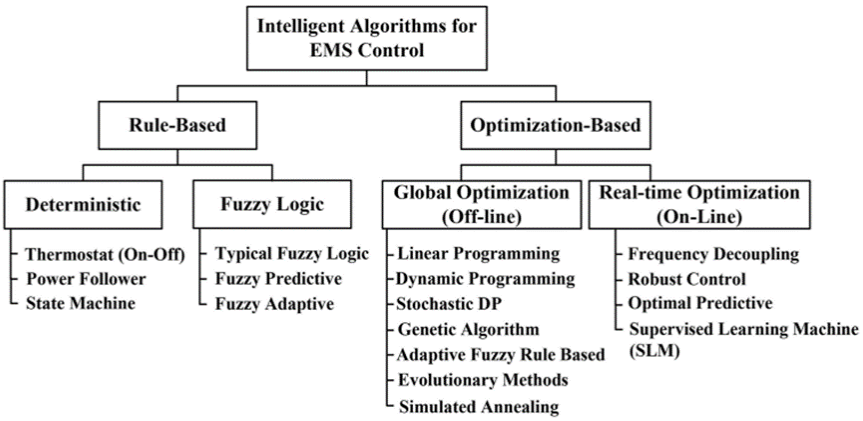

Figure 2.14: Classification of intelligent algorithms for EMS [6]

As can be seen from figure 2.14, algorithms for EMS control are categorized into two main classes: Rule-based and optimization-based.

- Rule-Based approaches: As the name itself suggests, in this type of approach the power demand is controlled by rules. These rules can be based on intuition, experiences, or mathematical models. This type of strategy has the advantages of low computational complexity, simple control, and high reliability. Rule-based approaches can be deterministic or fuzzy type. In deterministic rule-based control models of operation are determined on power demand. Fuzzy logical control (FLC) is a mathematical logic based on the degree of truth unlike true or false. This algorithm improved the control according to the prediction and the real demand power value. In addition, it can be divided into typical Fuzzy Logic, Fuzzy Predictive, and Fuzzy Adaptive.

- Optimization-Based approaches: This type of approach employs modern optimization algorithms with high complexity. The optimization problem can be solved using different algorithms such as Linear Programming, used if the system is convex and can be represented by a set of linear functions, Dynamic Programming (DP), in which it can determine the optimal control input via the design optimization objective function, DP is able to handle complex linear and non-linear systems, Stochastic DP, this DP control needs a large amount of data, especially in case of multiple states and multiple inputs, it may occur heavy calculation, Genetic algorithm, it a method of searching the optimal solution by simulating the natural evolution process, Model Predictive control, that depends on two aspects: the prediction accuracy and the optimization of the control strategy. For real-time optimization, the artificial intelligence (AI) algorithms are implemented. [16]

2.7.1 Equivalent Consumption Minimization Strategy (ECMS)

The above classification is missing one of the most commonly used hybrid control strategies: the equivalent consumption minimization strategy (ECMS). ECMS is a strategy based on the idea that the difference between the initial and final State of Charge of the battery must be very small with respect to the total energy used in an entire cycle. This means that the electrical energy used by the battery must be restored using the fuel tank or through regenerative braking. This leads to a cost function based on the energy taken from both the tank and the battery. Considering a specific operational condition, two scenarios can arise:

1. Discharge case when the battery power is positive. This implies that at a later time, the battery will discharge, resulting in additional fuel consumption required for recharging. The quantity of fuel needed is also contingent on the effectiveness of energy recovery via regenerative braking.

2. Charge case when the battery power is negative. This signifies that at some point in the future, this energy will be employed to supplement the overall energy required by the powertrain, leading to an immediate reduction in fuel consumption.

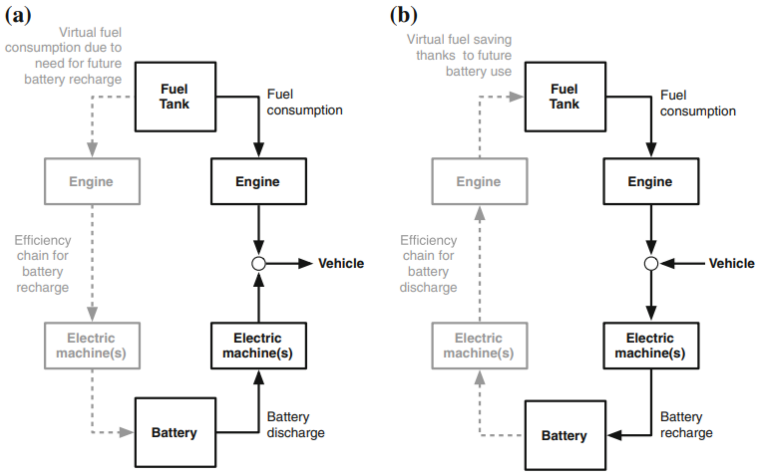

Figure 2.15: Energy path in the discharging phase (a) and in the charging phase (b) for a parallel HEV. [17]

The fundamental idea of ECMS is illustrated in figure 2.15.

The instantaneous equivalent fuel consumption associated with the electric energy is defined as:

$$\dot{m}_{f,eqv}(t) = \dot{m}_f(t) + \dot{m}_{ress}(t) \tag{2.1}$$

Where the real instantaneous total fuel consumption of the engine is:

$$\dot{m}_f(t) = \frac{P_{eng}(t)}{\eta_{eng}(t) Q_{lhv}} \tag{2.2}$$

Q_{lhv} is the fuel's lower heating value, $\eta_{eng}(t)$ is the engine efficiency, and $P_{eng}(t)$ is the power produced by the engine when it operates at a certain efficiency.

The virtual fuel consumed by the electric machine is calculated as:

$$\dot{m}_{ress}(t) = \frac{s(t)}{Q_{lhv}} P_{batt}(t) \tag{2.3}$$

$P_{batt}(t)$ is the battery power, $s(t)$ is an equivalence factor that assigns a cost to the use of electrical power. It is a vector composed by s_{charge} and $s_{discharge}$, two terms correlated by the relationship:

$$s_{charge}(t) = (\eta_{batt})^2 s_{discharge}(t) \tag{2.4}$$

where η_{batt} is the battery charge/discharge efficiency.

The optimization task is simplified into a local problem, focused on minimizing $\dot{m}feqv(t)$, as opposed to the broader problem of minimizing the total cost

$$\begin{cases} \min_{P_{batt} \in U_{P_{batt}}} \int_{t_0}^{t_f} \dot{m}_{f,eqv}(t)dt \\ \mathrm{SOC}_{min} \leq SOC \leq SOC_{max} \end{cases} \tag{2.5}$$

A multiplicative penalty function ($p(SOC)$)is used to ensure that SOC does not pass the imposed limits and it is defined as:

$$p(SOC) = 1 - \Big(\frac{SOC(t) - SOC_{target}}{(SOC_{max} - SOC_{min})/2} \Big)^a \tag{2.6}$$

This factor considers the difference between the current SOC and the desired SOC, and makes adjustments to account for it. There are three possible cases:

$$\begin{cases} \mathrm{SOC(t)} = \mathrm{SOC}_{target} \implies p(SOC) = 1 \\ \mathrm{SOC(t)} > \mathrm{SOC}_{target} \implies p(SOC) < 1 \\ \mathrm{SOC(t)} < \mathrm{SOC}_{target} \implies p(SOC) > 1 \end{cases}$$

The behavior of $p(SOC)$ depends on the choice of the exponent a. The total instantaneous equivalent fuel equation can be rewritten as:

$$\dot{m}_{f,eqv}(t) = \dot{m}_f(t) + \frac{s(t)}{Q_{lhv}} P_{batt}(t) p(SOC) \tag{2.7}$$

The selection of the parameter s is a pivotal aspect of ECMS, as its determination has a direct impact on both the battery SOC and fuel consumption.

In the conventional ECMS, the equivalence factor s remains fixed and is determined offline, relying on prior knowledge of the driving cycle. An alternative approach is the Adaptive ECMS, where the value of s is dynamically adjusted in real-time to align with the current driving patterns. Further details on this application are provided in the following section.

2.7.2 Adaptive ECMS

Adaptive ECMS (A-ECMS) is a real-time optimization technique that continuously adjusts the value of the equivalence factor s based on the target driving conditions.
In literature exist three different types of adaptation techniques:

1. **Adaptation based on driving cycle prediction**:
   The ECMS is combined with a module that establishes a connection between the present speed profile and the assessment of parameter s. Various methodologies are employed for this purpose.

2. **Adaptation based on driving pattern recognition**:
   This method relies on the premise that comparable driving patterns are associated with akin values of s.

3. **Adaptation based on feedback from SOC**:
   This approach is founded on the concept of adjusting the equivalence factor based on the SOC's deviation from the target value. These calculations are performed without the need for historical data or predictive driving pattern information.

Chapter 3

Methodology

3.1 Vehicle model overview

The vehicle considered in this thesis work is a 48V P1 mild-hybrid light-duty commercial vehicle implemented in MATLAB/Simulink/Simscape. There are different approaches to modeling hybrid vehicles. Among these, it is possible to distinguish two approaches based on the direction of the calculation method: Backward and Forward.

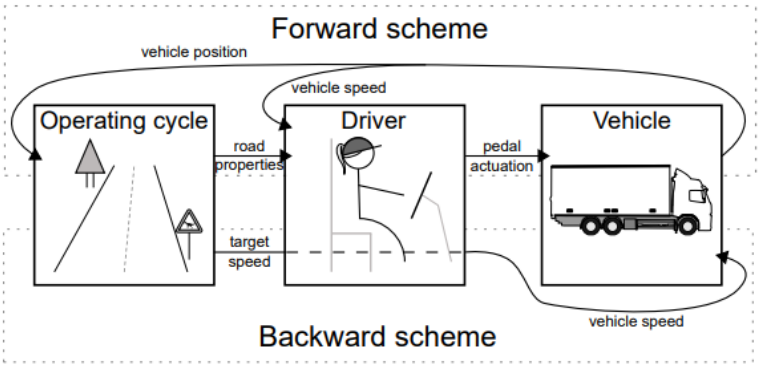

Figure 3.1: Backward and Forward approach [18]

1. **Backward approach**
   In this approach, the driving cycle provides a set speed, called target speed, and it's assumed that the vehicle follows this speed perfectly. The vehicle parameters evolve over time. The data flows

from the wheels to the powertrain.

2. **Forward approach**
   In this approach, the driving cycles provide a target speed, as in the previous method but no assumption is made for the vehicle speed. The data flows from the driver to the powertrain to the wheels.

The method used for modeling the vehicle implemented in Simulink is the forward one.

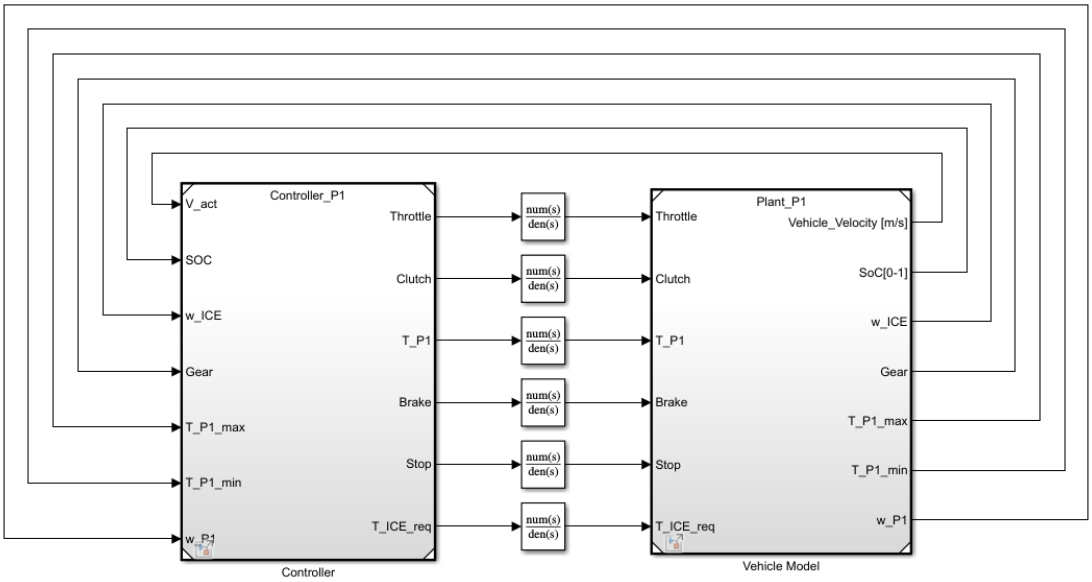

Figure 3.2: Simulink model

3.1.1 Plant

The Plant implemented in Matlab contains the vehicle model, tire model, and powertrain modeled in two dimensions.

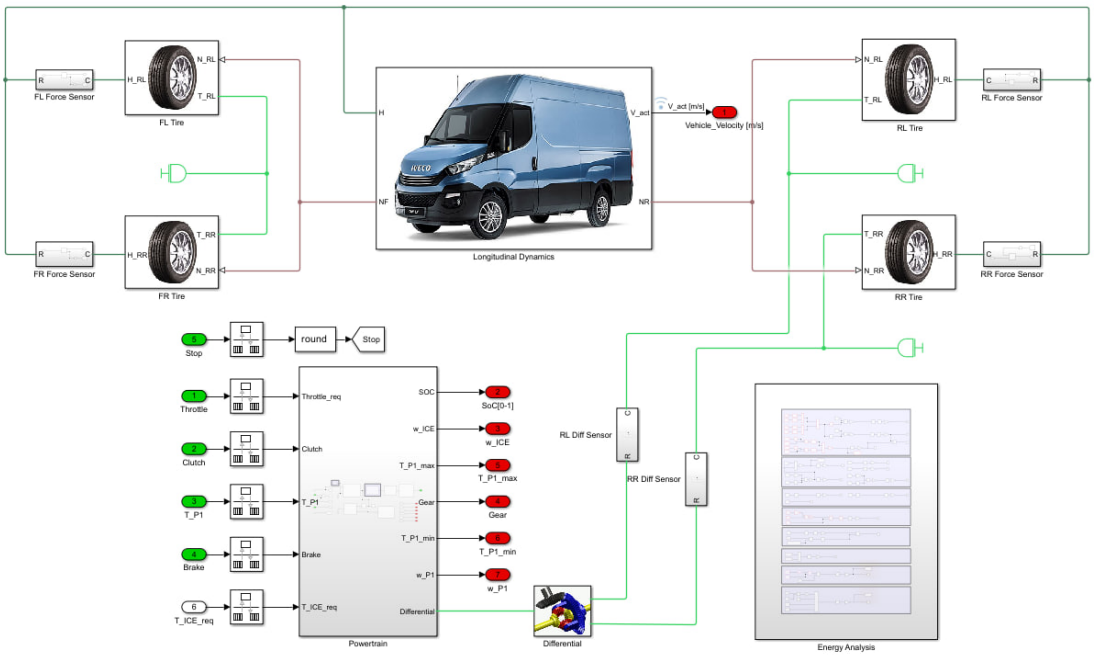

Figure 3.3: Plant

As shown in the figure 3.3, the longitudinal dynamics block contains the model of the vehicles schematized through a two-axle body in longitudinal motion which accounts for body mass, aerodynamics drag, weight distribution between axles, and road incline.

Powertrain model

From the figure 3.4 it is possible to observe that the electric motor is placed on the output of the crankshaft of the engine, directly connected to the ICE, so it is a P1 configuration.

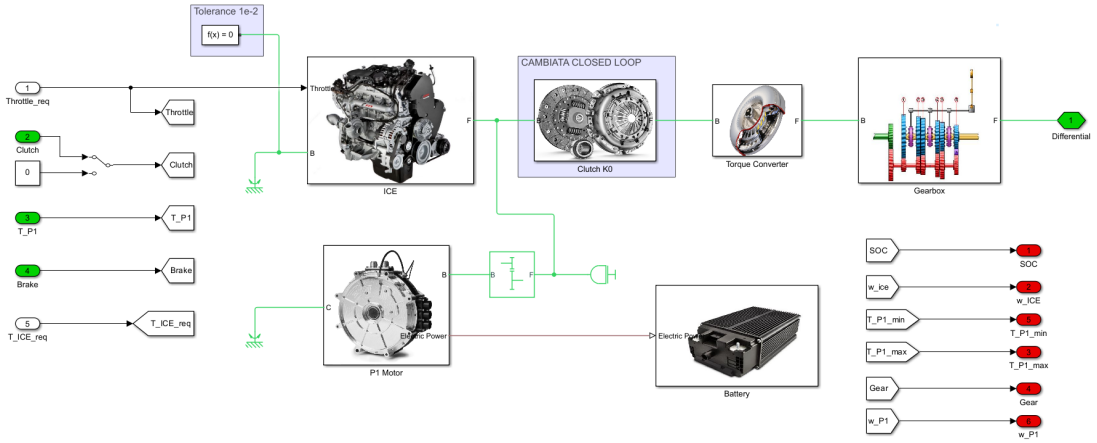

Figure 3.4: Powertrain

3.1.2 Energy Analysis

The focus of this thesis work is the improvement of energy management strategy, therefore it is important to understand the energy recovery potential and the losses from the energy point of view. In this way it is possible to observe where it is necessary to act to improve efficiency. This configuration of hybrid vehicle uses the engine as the primary source of power and the electric motor is used only to assist the ICE. Hence, the total energy needed for the traction of the vehicle is produced by the Internal Combustion Engine and P1 motors. The Electric Motor (EM) has two operating modes: for positive torques operates in motoring mode, and for negative torque the EM operates as a generator and produces electric energy that is stored in the battery. So, the total energy requested is calculated as:

$$E_{powertrain} = E_{ICE} + E_{P1,motor}$$

This energy goes to the driveline, more precisely it is transmitted to the torque converter and then goes to the differential. The driveline includes all the rotating elements and gears. The input energy should be equal to the energy that comes from the motors but due to the losses in the driveline, this energy is dissipated according to:

$$E_{powertrain} - E_{differential} = E_{driveline,losses}$$

The energy from the differential is transferred to the wheels and transformed into energy of motion, which is the energy needed by the wheels to move the vehicle. This energy should compensate for the energy dissipated due to aerodynamic resistance, rolling resistance, and potential energy, caused by the respective forces:

$$F_{aereodynamic} = \frac{1}{2}\rho_{air} A_f C_d v_{vehicle}^2$$
$$F_{rolling} = c_{roll}(v_{veh}, p_{tire}, ...) M_{vehicle} g cos\delta$$
$$F_{grade} = M_{vehicle} g sin\delta$$

Where ρ_{air} is the air density, A_f the vehicle frontal area, C_d the aerodynamic drag coefficient, g is the gravity acceleration, δ the road slope angle, and c_{roll} is a rolling resistance coefficient.

ρ_{air}	1.225
c_{roll}	0.0107
A_f	4.614
C_d	0.46
δ	0

Table 3.1: Values of dissipation forces coefficients

As it is possible to notice from the formulas above, the value of losses strictly depends on the velocity. The histogram 3.5 shows this behavior.

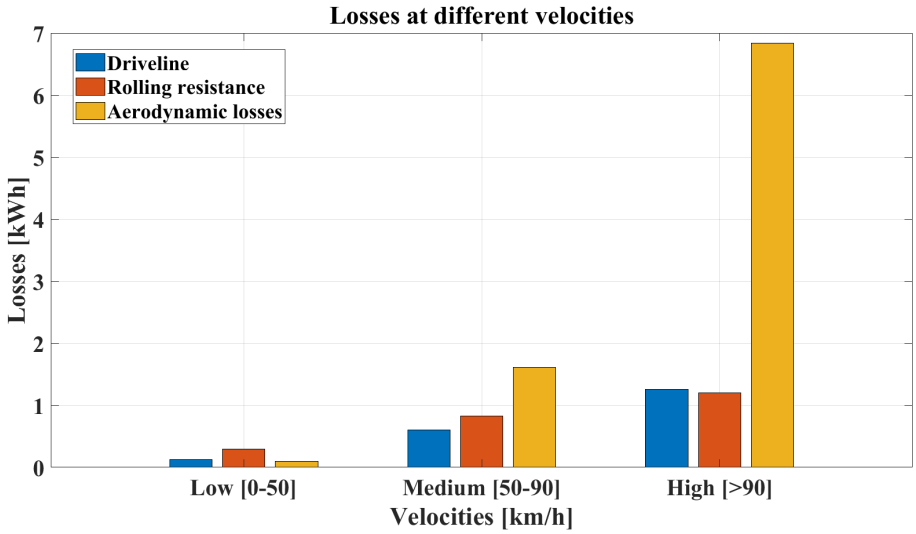

Figure 3.5: Losses at different velocities

The analysis is performed on complete driving cycles. The aerodynamic losses increase with high velocities, while at low velocities they are almost zero because the aerodynamic force is proportional to the square of the vehicle speed. A similar behavior is followed by the driveline losses that increase with increasing velocity. On the other hand, the losses due to rolling resistance are less relevant compared to the other losses.

Battery analysis

The characteristics of the battery are:

Nominal Voltage [V]	48
Cell Capacity [Ahr]	32
Nominal power [kWhr]	1.5

Table 3.2: Battery characteristics

The battery losses are computed as the difference between the output and the input power of the battery, where the input power is the electric

power coming from the P1 motor:

$$P_{batt} - P_{p1,el} = P_{loss}$$

Where:

$$P_{batt} = IV$$

The power of the P1 motor can be divided between electric and mechanical, defined as:

$$\begin{cases} \mathrm{P}_{p1,el} = P_{p1}\eta_{em}^{sign(-P_{p1})} \\ \mathrm{P}_{p1,mec} = T_{p1}\omega_{p1,mec} \end{cases}$$

The difference between the mechanical and electric power of P1 is the losses of the electric motor

$$P_{p1,mec} - P_{p1,el} = P_{loss,em}$$

An important parameter for battery analysis is the C-rate. A C-rate is a measure of the rate at which a battery is discharged relative to its maximum capacity. Knowing that the battery has a capacity of 32 Ah, it can discharge 32 A of current in 1 hour or, similarly, considering the nominal energy of 1.5 kWh it can discharge 1.5 kW in 1 hour. In the model used for this work a maximum C-rate is around 17C. However, the current is limited by the power electronics to around 400A, so we can assume a maximum C-rate of 15C.

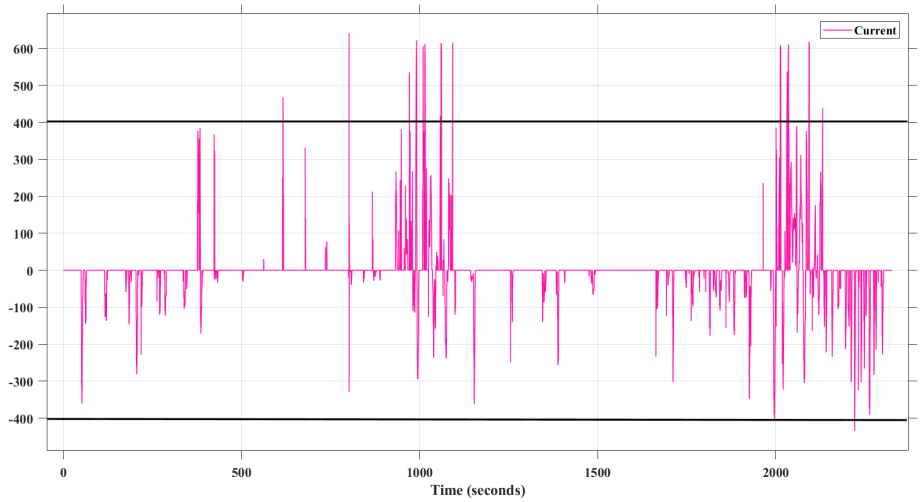

Figure 3.6: Current limitation

In the figure 3.6 there are many points where the current goes beyond the limits of 15C, these points correspond to sudden changes in the slope of the acceleration.
The vehicle under examination is a 48V P1 mild-hybrid, which exhibits high current demands owing to its 48V system voltage. To address this, potential solutions involve current limitations, using higher-performance components, or integrating a supercapacitor.
In this thesis, two distinct approaches are investigated. The first assesses the viability of a Hybrid Energy Storage System (HESS) comprising a supercapacitor in parallel with the primary battery. The second approach focuses on enhancing the Energy Management System (EMS) by accounting for battery thermal characteristics and State-of-Health estimation.

3.1.3 Controller

The controller in figure 3.7 consists of a high lever controller in which the driving cycles give the driver the reference speed profile. The driver is modeled as a PI controller. The output of this controller is the throttle which is further converted into torque and supplied to the

control strategy. The subsequent control approach strives to determine the most efficient power distribution between the electric motor and the internal combustion engine. Therefore there are different operating modes: ICE only or Hybrid mode. For the Hybrid mode, there are different approaches, the one applied in this work is the ECMS described in chapter 2.7.1.

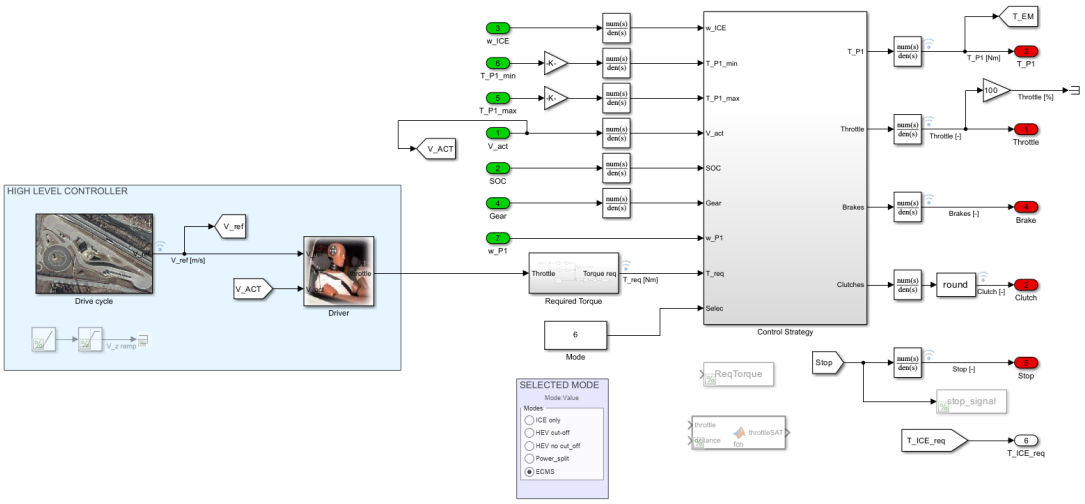

Figure 3.7: Controller

As mentioned previously, the control strategy takes torque as its input, which can be either positive or negative.

- If the torque is negative means that the electric motor works as a generator and produces electric energy used to recharge the battery.

$$T_{requested} < 0 \Rightarrow T_{requested} = T_{P1,generator}$$

- If the torque is positive means that the electric motor works as a motor and it assist the ICE to supply the total requested torque.

$$T_{requested} > 0 \Rightarrow T_{requested} = T_{P1,motor} + T_{ICE}$$

This strategy also manages the battery energy storage. An initial differentiation that needs to be made involves distinguishing between

charge-sustaining (CS) and charge-depleting (CD) modes.
In CS mode, the vehicle's battery is discharged by the electric motor during startup and boost operations, and it is recharged during regenerative braking to maintain the battery within a predefined state of charge limits.
In CD mode, the battery is discharged more than it is replenished by the generator or regenerative braking, resulting in a lower final SOC compared to the initial target.

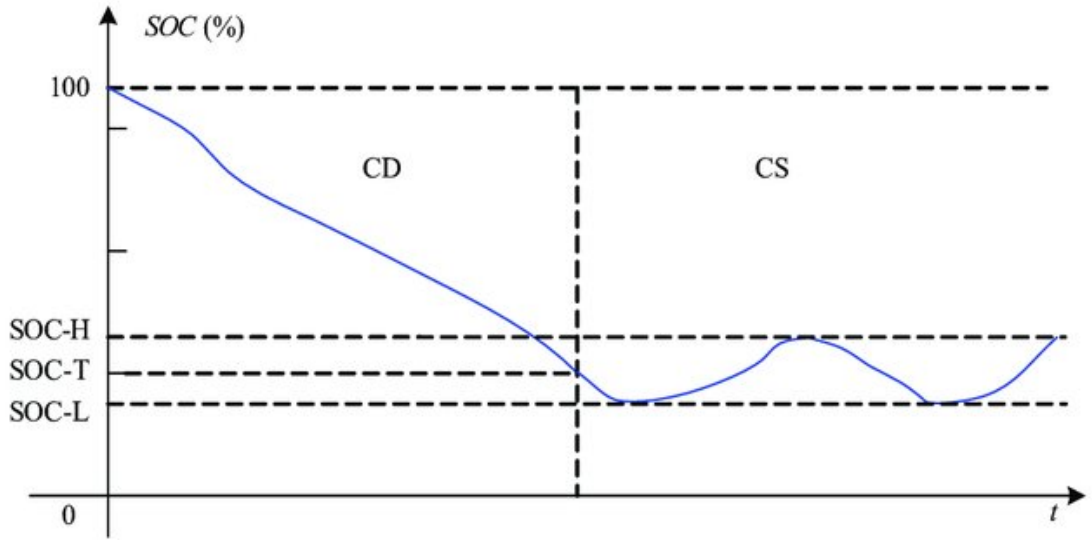

Figure 3.8: Charge Sustaining and Charge Depleting [19]

In the analyzed model, the battery is in charge-sustaining mode and the imposed limits for SOC are 56% and 64% because the required target is 60% .

As mentioned before in paragraph 2.7.1, the equivalent factor s is an important parameter for ECMS. In this case, s is set taking into account the limitation for the SOC of the charge-sustaining mode. It is modeled as a rely.
This relay activates when the State of Charge (SoC) exceeds the upper threshold of 64%. Once activated, the relay remains on until the lower threshold of 56% SoC is reached. It remains off until the upper threshold is reached again.

The equivalence factor, determined through this process, serves as an input to the ECMS, which can adjust the torque distribution based on the SoC. When the SoC surpasses 64%, only the P1 motor provides torque to bring the SoC within the desired range. Conversely, when the SoC falls below 56%, only the internal combustion engine (ICE) contributes to the torque to recharge the battery.

3.2 Batteries modeling

Researchers have developed different battery models based on different levels of accuracy and complexity. Generally, we can classify these models into three categories: White-box models, Grey-box models, and Black-box models. An example of the white-box model is the Electrochemical model, this model uses physical law that governs the internal electrochemical process of the battery, moreover, it takes into consideration several non-equilibrium effects involving high power density and high-density power source. However, to use the electrochemical models for simulation, many parameters based on in-depth knowledge of the battery's chemical structure and properties, such as chemical composition and material conductivity, need to be measured or known, which is impractical for many system design engineers [15]. On the other hand, examples of Grey-box models are equivalent electric circuit models (EECMs) and reduced-order models. The first one use a combination of a voltage source, resistors, capacitors, and sometimes non-linear elements to describe battery behavior. To avoid complex analysis of non-linear elements, such as the Warburg impedance, it has been proposed in [15] to use a linear EECM structure, consisting of an ideal voltage source representing the open circuit voltage (OCV) which is controlled by state of charge (SOC) and temperature, a resistor representing for the internal resistance, and a few RC networks connected in series to capture the dynamics of the battery behavior. Such a linear EECM is defined as a n-th order if it consists of n-series RC networks. The latter is based on the electrochemical model shown before by making additional assumptions that simplify the battery model, however, models result in a heavy loss of information compared

with the complete electrochemical model. Black-box models describe battery behavior using some intelligent modeling methods without the need to understand the electrochemical processes in the battery.

3.2.1 Equivalent electric circuit models (EECMs)

The circuit model is the one that will be taken into consideration later in this thesis work. Different categories of equivalent circuits will be analyzed below.

- **Ideal model**
  The battery is represented by an ideal voltage generator, the internal parameters and state of charge are ignored. This makes it the simplest battery model.

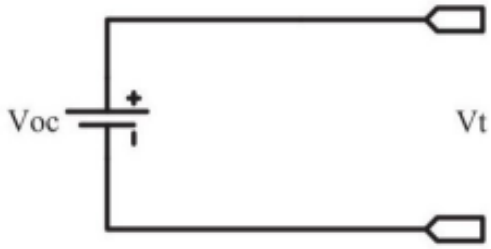

Figure 3.9: Ideal model [20]

- **Simplified model**
  This model is composed of an ideal voltage generator with a resistor in series which represents the internal resistance of the battery. As in the previous model, the state of charge is not considered. In the figure 3.9 V_{oc} is the ideal open circuit voltage while V_t is the measured voltage.

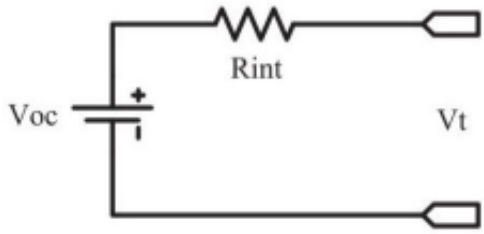

Figure 3.10: Simplified model [20]

- **Simplified model I**
  This is still a simplified model but compared to the previous one, in this one, the internal resistance and the voltage are functions of the state of charge. The internal resistance is calculated in this way:

$$Rint = \frac{R_0}{S_k}$$

  Where R_0 is the initial internal resistance and S_k is the initial battery state of charge.

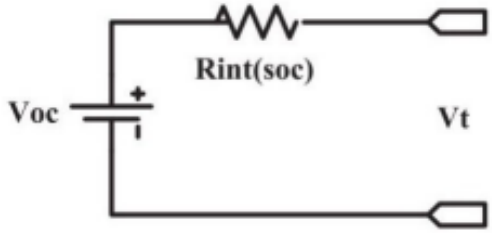

Figure 3.11: Simplified model I [20]

- **Simplified model II**
  This is a model similar to the previous one, in fact in this model the voltage and the internal resistance is a function of the state of charge. The difference is in the relationship that describes the open voltage circuit:

$$V_t = V_{oc}(SOC) - IR_{int}(SOC)$$

Where $V_{oc}(SOC)$ is the no-load voltage of the battery and $R_{int}(SOC)$ is the internal resistance of the charge and discharge cycle.

$$V_{oc} = V_0 - AD$$
$$R_{int} = R_0 - BD$$

Where V_0 is the open circuit voltage with the battery fully charged, D is the state of discharge, *Rint* is the internal resistance with the battery fully charged and A and B are constantly obtained from experimental tests [20].

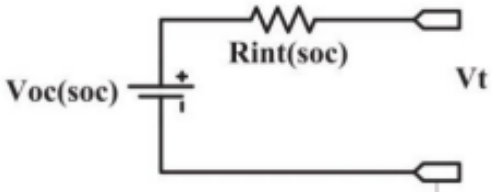

Figure 3.12: Simplified model II [20]

- **Simplified model III**
  This model is based on the Thevenin model in which the open circuit voltage and the internal resistance have a non-linear relation:

$$V_t = V_{oc} - (R_{int} + \frac{K}{SOC})I$$

where K is the polarization constant and I is the discharge current

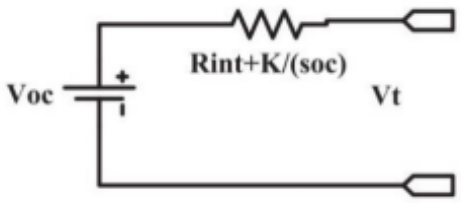

Figure 3.13: Simplified model III [20]

- **Simplified model IV**
  As shown in figure 3.14, this model has more than one voltage source in series with the internal resistance.

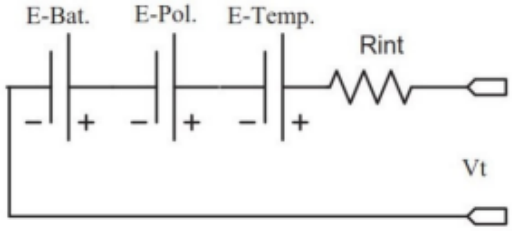

Figure 3.14: Simplified model IV [20]

Where E-Bat is the ideal source of the battery cell, E-pol shows the polarization effect on the battery, and E-Temp shows the thermal effect on the battery.

- **Thevenin model**
  All the previous models do not take into account the dynamic effect of the battery. To analyze transient conditions, Thevenin add to the equivalent circuit an RC circuit. The simplest Thevenin model is shown in the figure 3.15 below.

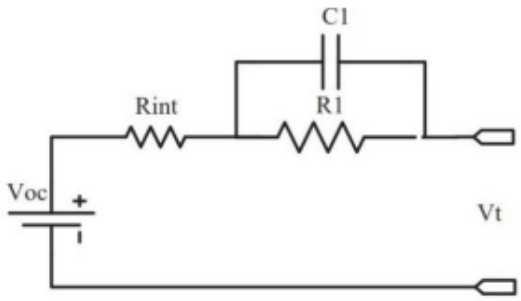

Figure 3.15: Thevenin model [20]

In this model, all the parameters are assumed as constant but in literature, there are different modified Thevenin models in which state of charge, temperature, and other values are tacked into account.

3.3 Supercapacitors modeling

Various models are elaborated and discussed in the literature, in terms of model structure, complexity, and accuracy for electrical behavior simulation, which are sorted into four groups: electrochemical, equivalent circuit, intelligent, and fractional-order models [21]. Electrochemical models offer high accuracy but increase complexity. This model is also known as a double-layer model due to the capacitor structure described above. Equivalent circuit models derive from empirical and experimental data, this circuit employs parameterized RC (capacitor-resistor) networks to mimic the electrical behavior of SCs. Intelligent circuit models predict the performance of energy storage systems. Fractional-order models consist of non-integer order differential equations and they are able to capture the SC dynamics. According to [12], the structural simplicity and decent modeling accuracy make the equivalent electrical circuit model very suitable for power electronic applications and real-time energy management simulations.

3.3.1 Equivalent circuit models

Over the years, many methods of modeling supercapacitors have been studied through the appropriate interconnection of RC circuits. The most used ones will be explained below:

- **RC series model**
  This is the easiest model used to have a general overview of the component's behavior. It consists of a capacitance and a resistor in series. Unfortunately, this model does not take into account the self-discharge phenomena and it cannot accurately represent charging and discharging cycles.

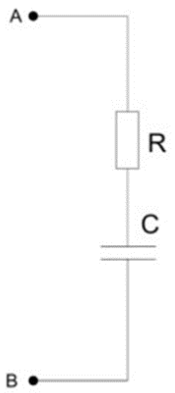

Figure 3.16: RC series model

- **Two-branch model**
  As the name suggests, it is composed of two branches; The first one consists of a capacitor that is the sum of two terms: a constant one and a voltage-dependent one, and a resistance that is one that acts as Equivalent Series Resistance (ESR). The second branch represents the medium-long term. The third branch represents the phenomenon of self-discharge. This model is used for representations of generally shorter periods.

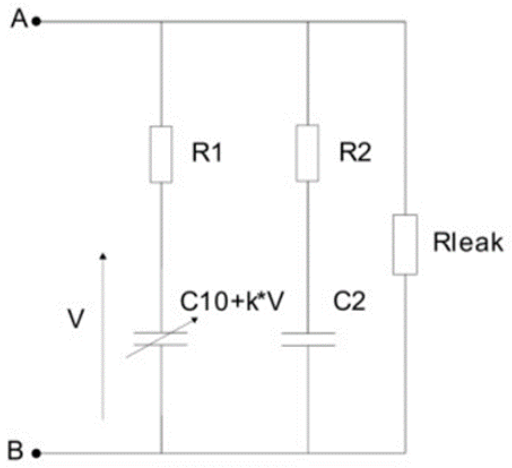

Figure 3.17: Two-branch model

- **Zubieta-Bonert model**
  In this model, there are three groups of RC circuits and one resistor connected to each other in parallel. Every RC branch has its own time constant.

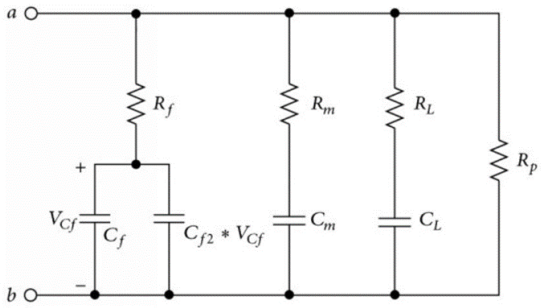

Figure 3.18: Zubieta-Bonert model

As in the previous model, the last branch represents the phenomenon of self-discharge. In the first branch, called the immediate or short-term branch, R_f dominates the behavior in the order of a few seconds, and C_{f2} represents the voltage dependence from the double layer capacity. The second branch, called the delayed or medium-term branch, with R_L, influences behavior in the minute

range. The third, the long period branch influences the response of the circuit after a time of ten minutes. This model is very good at low frequencies but not very good at high ones.

- **Musolino-Piegari model**
  In [22], a full-frequency-range model that can be used to represent all of the phenomena that involve supercapacitors. Moreover the authors present a simple procedure to identify the parameters of the model that can be used to characterize this supercapacitor.

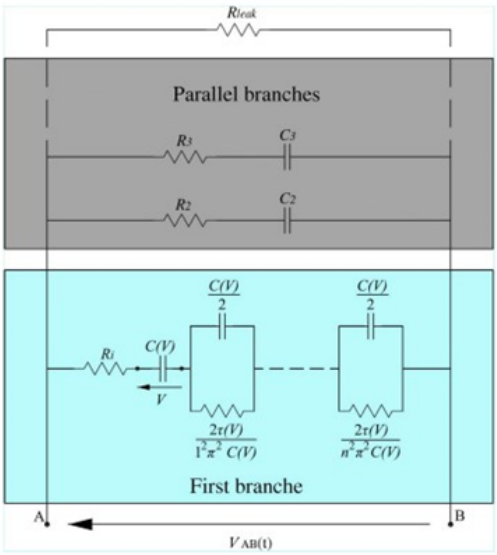

Figure 3.19: Musolino-Piegari model

All the elements of the first branch depend on the three parameters: R_i, C, and τ; the last two are voltage-dependent parameters. For slow dynamics, the number of parallel branches should be infinite. However, two parallel branches are sufficient to achieve accurate results. Finally, a resistor R_{leak} is added to model the self-discharge phenomenon.

- **RC Transmission Lines Model**
  The RC transmission line model is based on the Porous Electrode

Theory developed by de Levie. According to this theory, each pore is modeled as one transmission line. This leads to a ladder network with potentially many RC elements.

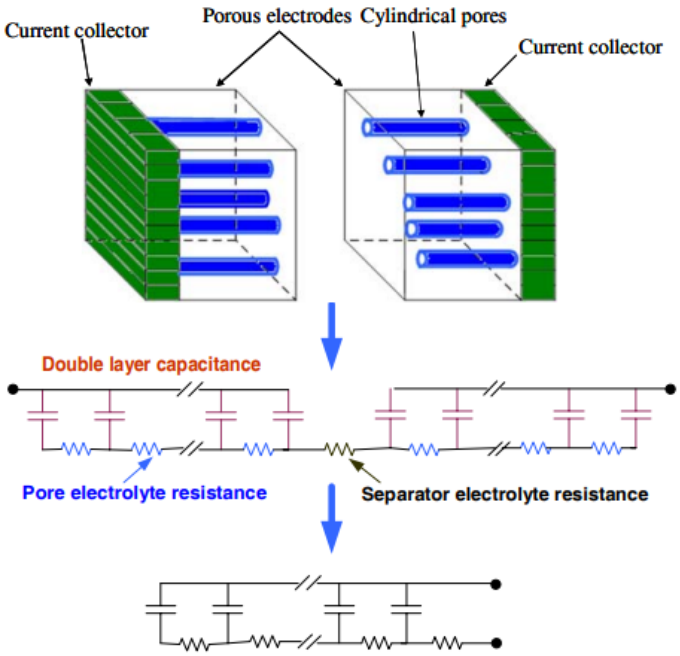

Figure 3.20: RC Transmission Lines Model

The transmission line model attempts to capture the distributed double-layer capacitance and the distributed electrolyte resistance that extends the depth of the pore [23].

3.4 Thermal dependence

Under varying environmental conditions, it may be necessary to either dissipate or introduce heat to regulate the battery's temperature and keep it within the ideal range. An uneven temperature distribution can lead to reduced charging and discharging efficiency and cell imbalances over time. Established methods for thermal management encompass the use of coolants, insulating materials, and phase-change substances. Integral tools in the design and thermal control of automotive battery

packs are thermal and performance models. These models rely on input data, including system and operational parameters. However, not all of these parameters are straightforward to directly measure (e.g., heat effects) because their impacts cannot be isolated.

3.4.1 Lumped thermal network model

The lumped thermal network model for the battery cell is illustrated in 3.21. The type of Li-ion battery taken into account in this work is a prismatic NMC battery cell.

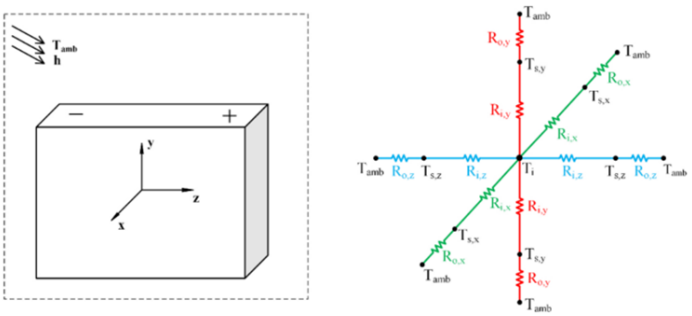

Figure 3.21: Lamped thermal model of prismatic NMC battery cell [24]

The model consists of various nodes that symbolize different components, including the inner core of the battery, its external faces, and the surrounding ambient temperature. The heat generated within the battery's core is conducted through the material to the faces, from where it is then released into the surroundings through convection [24].

Heat generation

The heat produced within the battery cell due to electrochemical reactions and the movement of ions in the electrolyte can be described by considering the local internal resistance and current densities. According to the theory, the total heat generated is calculated as:

$$mC_p\frac{dT(t)}{dt} = k[Ri^2(t)] - (Q_{conv} + Q_{rad}) \tag{3.1}$$

m is the cell mass, C_p is the specific heat capacity, T is the cell temperature, i is the charge/discharge current, R is the internal resistance of the cell, k represents the scaling factor that accommodates the variation in electrical conductivity between the positive and negative electrodes, Q_{conv} is the convection heat energy, Q_{rad} is the radiation heat energy. In ideal conditions, R can be defined as a fixed value but in reality, it can be expressed as a function of battery State-of-Charge (SOC), as shown in figure 3.22, or as a function of temperature, as shown in figure 3.23.

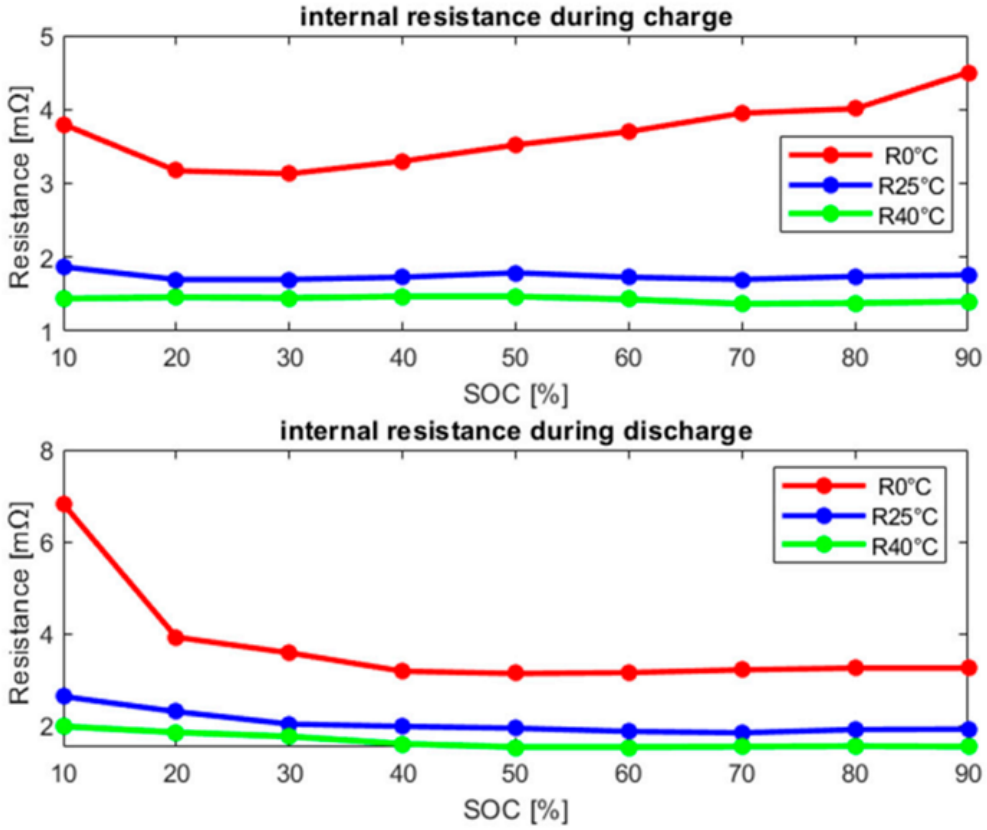

Figure 4. Electrical resistance as a function of SOC and temperature.

Figure 3.22: Internal resistance of battery cell as a function of SOC [25]

Notably, the charge resistance is lower than the discharge resistance, indicating that less Joule heat is generated during the charging phase.

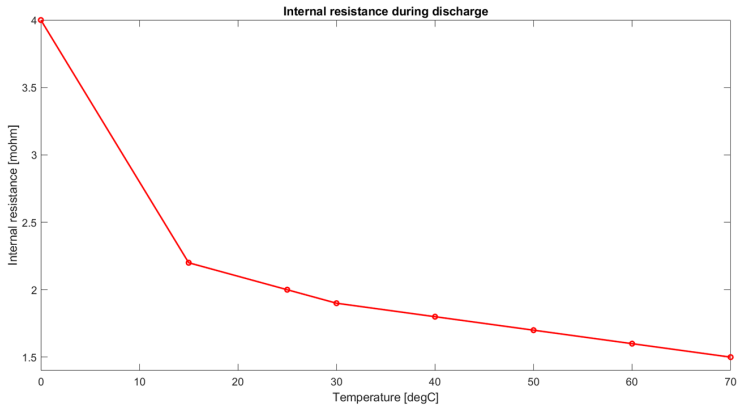

Figure 3.23: Internal resistance of battery cell as a function of temperature

A typical trend of R with SOC and T for a lithium cell is studied in [26] and it is depicted in the illustration 3.24:

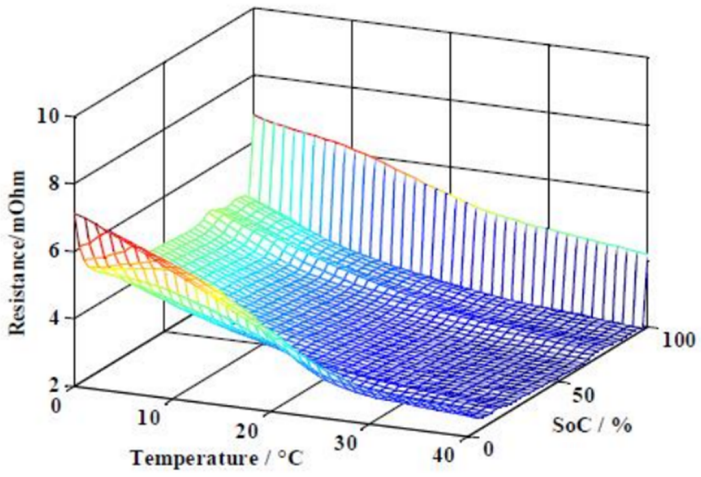

Figure 3.24: Internal resistance of battery cell as a function of temperature and SOC

The data in figure 3.24 illustrates the variations of the internal resistance concerning the State of Charge (SOC) and temperature. Consequently, as elaborated in Chapter 3.1.3, the battery under examination operates in a charge-sustaining mode, and due to the applied strategy, the SOC operates within the range of 50% to 70% to achieve the desired target of 60% and the temperatures taken into consideration will be 25, 30 and 40 $°C$. This results in a relatively stable internal resistance.
As with R V_{oc} in an ideal condition is defined as a fixed value but in reality, it can be expressed as a function of battery State-of-Charge (SOC) or temperature. This relations are illustrated in 3.25 and 3.26.

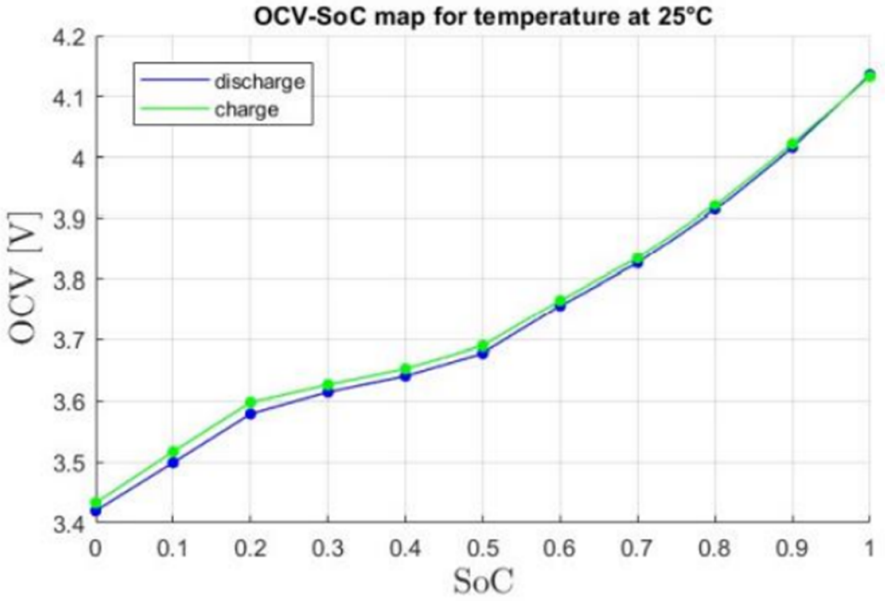

Figure 3.25: OCV of battery cell as a function of SOC

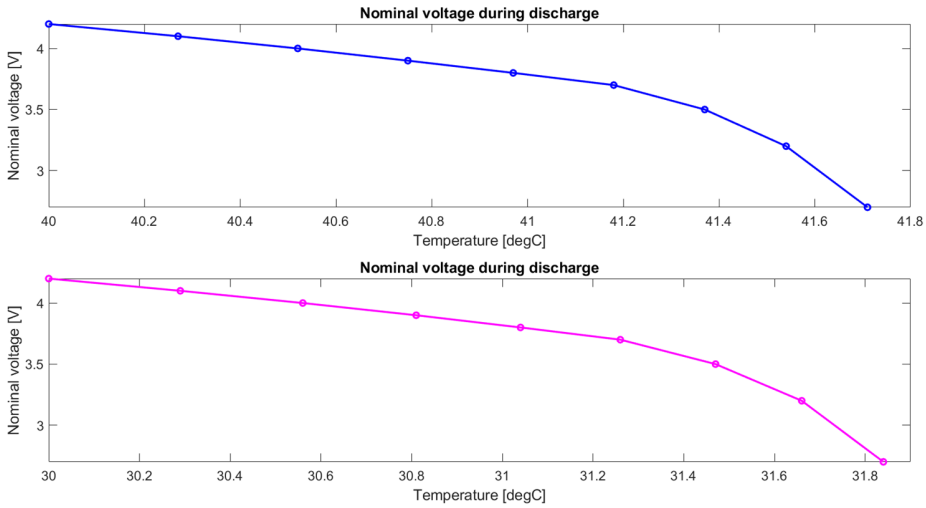

Figure 3.26: OCV of battery cell as a function of temperature

In figure 3.26 the first graph refers to the voltage measured with an exchange temperature equal to 40 $°C$ and the second with the exchange temperature equal to 30 $°C$.
The heat transfer through convection, denoted as Q_{conv}, at the surface of the battery cell, can be represented as follows:

$$Q_{conv} = hA(T_s - T_c) \tag{3.2}$$

where h represent the convective heat transfer coefficient, A is the area of battery cell, T_s is the surface temperature of the cell, T_c is the temperature of cooling air.
The heat transfer coefficient (h) is strongly linked to the cooling valve's power within the battery module. A high coefficient necessitates a larger cooling valve with a correspondingly higher power requirement. Therefore, the higher 'h' is, the more energy will be consumed.
The study in [27] examined the ideal heat transfer coefficient between the battery and the surrounding ambient temperature. The findings indicate that the heat transfer coefficient exhibits a cubic relationship with the ambient temperature. For instance, when the ambient temperature is 30$°C$, the heat transfer coefficient should be a minimum of 12 W/m^2K.

Modeling conditions

Properties of the cells, including density, thermal conductivity, and specific heat capacity, are presumed to be constant across the entire battery and to stay within a predefined temperature range. The values of these parameters used for the model under consideration will be illustrated in the next chapter.
In this study, we operate on the assumption that the heat exchange by convection takes place on a well-defined surface. This simplification is used which consists of modeling the battery as a single body to simplify the model.

3.4.2 Matlab model

The battery was modeled in Matlab Simscape environment.This particular software enables the creation of physical component models using physical connections, which can then be linked through block diagrams within Simulink.
The previous model of the battery is made up of the fundamental battery model in Simscape as shown in figure 3.27.

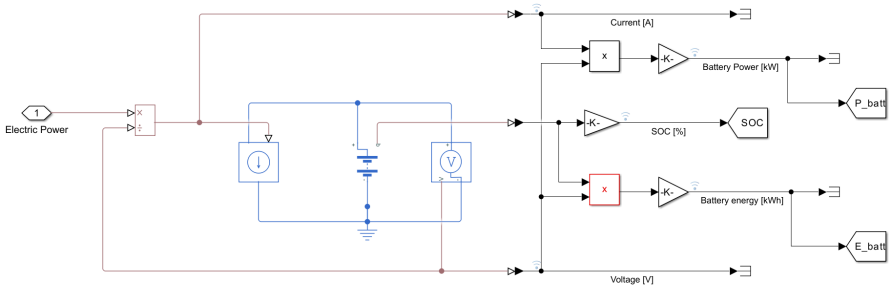

Figure 3.27: Battery model

Through the use of this Matlab block, the battery is represented by a combination of a series resistor and a voltage source that varies with charge. The voltage is dependent on the charge and follows this

relationship:

$$V = V_0 \frac{SOC}{1 - \beta(1 - SOC)} \tag{3.3}$$

Where SOC is the State of Charge (how the SOC is calculated is explained in chapter 2.6.2), V_0 is the nominal voltage, β is a constant that is calculated so that the battery voltage is V_1 when the charge is AH_1, V_1 is the voltage measured when the charge is AH_1, AH_1 is the charge measured when no-load volts are V_1 .
This equation offers an estimation of the voltage as it relates to the remaining charge. This approximation mimics the rapid decline in voltage as charge levels decrease, and it guarantees that the battery voltage reaches zero when the charge is fully depleted. The model's benefit lies in its simplicity, as it relies on only a small number of parameters, typically found on most datasheets. By utilizing this model, it becomes feasible to assess the battery's State of Charge (SOC), which is then provided as feedback to the controller.
One of the goals of this thesis is to consider the thermal aspect of the battery. Adding this aspect to the previous battery model the voltage equation will become:

$$V = V_{0T} \frac{SOC}{1 - \beta_T(1 - SOC)} \tag{3.4}$$

$$V_{0T} = V_0(1 + \lambda_V(T - T_1)) \tag{3.5}$$

where T is the battery temperature, T_1 is the nominal measurement temperature, λ_V is the parameter temperature dependence coefficient for V_0 , β_T is calculated as:

$$\beta_T = \beta[1 + \lambda_\beta(T - T_1)]$$

λ_β is the parameter temperature dependence coefficient for β, β is calculated in the same way of 3.3 using V_{0T}.
All the coefficients related to temperature dependence are calculated based on the provided values at both the nominal and the second measurement temperatures

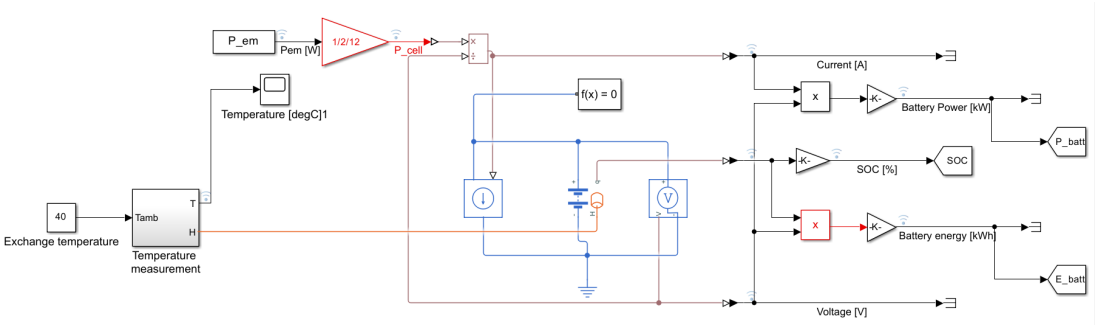

Figure 3.28: Battery model with thermal dependence

The battery temperature is provided by:

$$M_{th}\dot{T} = \sum_{i} \frac{V_{t,i}^2}{R_{t,i}} \tag{3.6}$$

Where M_{th} is the battery thermal mass, i corresponds to the ith ohmic loss contributor that in the analyzed model corresponds to series resistances and self-discharge resistance, $V_{T,i}$ is the voltage drop across resistor i, $R_{T,i}$ is resistor i.
The block uses linear interpolation for the derived equation coefficients. All the coefficients given as input to the thermal part of the battery come from "Temperature measurements" block illustrated in figure 3.28.

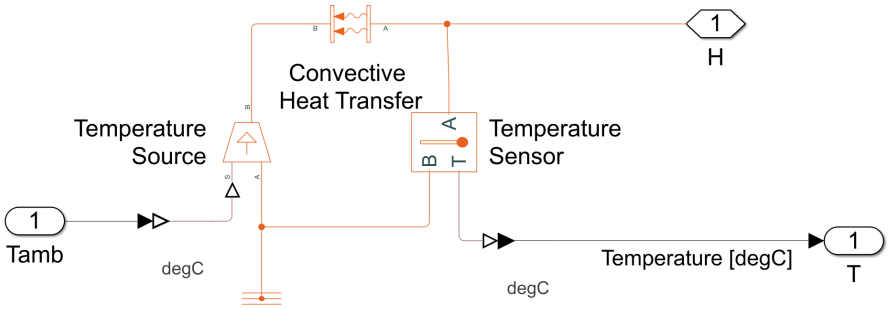

Figure 3.29: Temperature measurements block

The block shown in figure 3.29 receives as input the constant value of the exchange temperature which is the temperature of the cooling system, it is sent to the ideal temperature source block that simulates

an ideal thermal energy source that maintains specified temperature difference across the source regardless of the heat flow consumed by the system. The temperature differential is sent to the convective heat transfer block that describes heat transfer between two bodies through fluid motion and represents it as convection. This heat transfer process is explained by Newton's law of cooling:

$$Q = kA(T_A - T_B) \tag{3.7}$$

where Q is the heat flow, k is the convection heat transfer coefficient, A is the surface area, T_A and T_B are the temperature of the two bodies. The heat flow is also equal to the power dissipated over the time:

$$Q = P_{diss}t \tag{3.8}$$

Substituting 3.7 into 3.8 :

$$P_{diss}t = hA\Delta T \tag{3.9}$$

The power dissipated in the battery model is an electrical power and is calculated as:

$$P_{diss} = RI^2 \tag{3.10}$$

In conclusion, substituting 3.10 in 3.9 the previous equation becomes:

$$RI^2t = hA\Delta T \tag{3.11}$$

Hence, the output temperature of this block is calculated as:

$$T_A = T_B + \frac{Q}{KA} \tag{3.12}$$

Where Q is calculated as in 3.8 and it is sent to the battery.

3.5 SOH Estimation

It's crucial for a battery to maintain a proper State of Charge (SOC) and State of Health (SOH) for various reasons. It's important to keep

track of two key factors.
SOC refers to the amount of charge currently stored in the battery, while SOH reflects the overall condition of the battery over time. A decrease in SOH can indicate a decline in the battery's ability to store and release energy, which can negatively impact its overall performance. Properly monitoring and managing SOC and SOH is crucial to maximize the lifespan of the battery and ensure reliable long-term performance.

As mentioned in 2.6.2, the State of Health is calculated as:

$$SOH\% = 100\frac{R_{EOL} - R_0}{R_{EOL} - R_{new}}$$

As seen in the previous formula, the internal resistance R_0 is an important indicator of the aging of a battery.
To determine the State of Health (SOH), a Simulink block in Matlab is employed. This block takes the SOC estimation, R0, and the measured temperature as inputs. The temperature is calculated in the same manner as in the prior model illustrated in the previous paragraph. The remaining two parameters are derived from a separate Matlab/Simulink block, which employs a Kalman filter algorithm to estimate the State of Charge (SOC) and the terminal resistance of the battery.

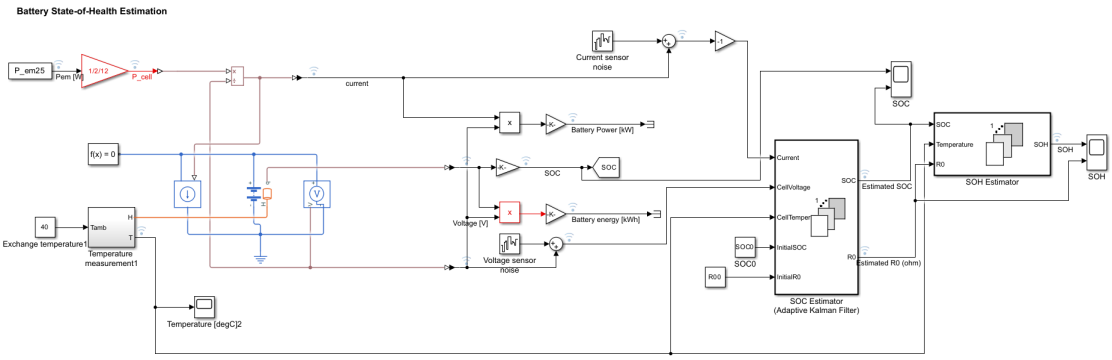

Figure 3.30: SOH estimation battery model

3.5.1 Kalman Filter

The widely used filtering technique is the Kalman filter, which processes a sequence of measurements collected over time, corrupted by statistical noise, to generate estimates of unknown variables. The algorithm begins with an initial prediction step, relying on prior knowledge of the state to be estimated, and then proceeds to an update or correction step, where the predicted state is adjusted based on the innovation introduced by the current measurements.
The system under examination is built upon non-linear Kalman filtering methods, which expand the application of Kalman filters to non-linear systems.

More specifically, the Matlab block employs these state variables as non-linear functions:

$$x = [SOC, V_1, R_0]$$

and this process and observation of nonlinear functions:

$$h(x, i) = V_0(SOC, T) - iR_0 - V_1$$

$$f(x, i) = \begin{bmatrix} -\frac{i}{3600AH(T)} \\ \frac{i}{C_i(SOC,T)} - \frac{V_1}{R_1(SOC,T)C_1(SOC,T)} \\ 0 \end{bmatrix}$$

The most common approach to applying Kalman theory to non-linear systems is the Extended Kalman filter (EKF). The EKF algorithm involves linearizing non-linear functions using a Gaussian random variable (GRV), which is then advanced through a first-order linearization of the non-linear system via Taylor expansion. However, a challenge with this propagation through the dynamics of non-linear systems is that it can introduce significant errors in the mean and covariance of the transformed GRV, potentially leading to filter divergence.
To address the limitations of the EKF, the Unscented Transformation

(UT) was developed as a method for propagating mean and covariance information through non-linear transformations. Consequently, the Kalman filter utilized in this battery model is the Unscented Kalman filter (UKF). Notably, the computational complexity of the UKF is in the same order as that of the EKF.

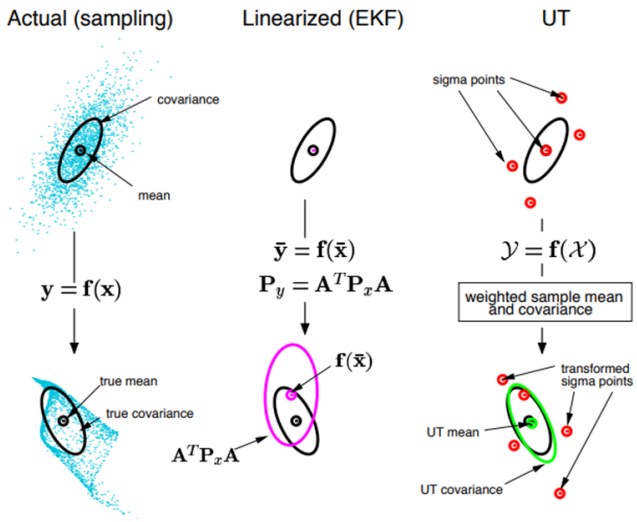

Figure 3.31: Example of the UT for mean and covariance propagation. a) actual b) first-order linearization c) UT [28]

The Unscented Kalman Filter (UKF) approximates the state distribution with a Gaussian random variable (GRV), much like the Extended Kalman Filter (EKF). However, in the UKF, this distribution is represented using a minimal set of strategically selected sample points known as σ-points. These σ-points fully encapsulate the actual mean and covariance of the GRV. When these points are propagated through the genuine non-linear system, the filter can accurately capture the posterior mean and covariance up to the third-order Taylor series expansion for any non-linearity. The σ-points and their associated weights are defined as:

$$\chi^{[0]} = \mu\chi^{[i]} = \mu + (\sqrt{(n+\lambda)\Sigma)_i} \qquad for\ i = 1, .., n$$

$$\chi^{[i]} = \mu - (\sqrt{(n+\lambda)\Sigma)_{i-n}} \qquad for\ i = n+1, .., 2n$$

$$w_m^{[0]} = \frac{\lambda}{n+\lambda}$$

$$w_c^{[0]} = w_m^{[0]} + (1 - \lambda^2 + \beta)$$

$$w_m^{[i]} = w_c^{[i]} = \frac{1}{2(n+\lambda)}$$

Where λ is calculated as follow:

$$\lambda = \alpha^2(n+k) - n$$

The distribution of σ-points relative to the mean state value is governed by two parameters, α and k. A third parameter, β, influences the weights applied to the transformed points when calculating state and measurement covariances.

- $\alpha \rightarrow$ is a coefficient that regulates the dispersion of σ-points. It falls within the range $0 < \alpha \leq 1$. Lower values result in sigma points positioned closer to the mean state.

- $\beta \rightarrow$ is a distribution coefficient with a minimum value of 0 or greater. In the case of a Gaussian distribution, its optimal value is 2.

- $k \rightarrow$ A secondary scaling parameter. σ-points are positioned closer to the mean state with smaller values. The calculation for k is as follows:

  $$k = 3 - n$$

  where n is the number of states.
  The complete formulation of the UKF algorithm is presented in figure 3.32, with the reference [29].

Algorithm 2 Unscented Kalman Filter $(\hat{x}_{t-1|t-1},\ \Sigma_{t-1|t-1},\ u_t,\ z_t)$

1: $\chi_{t-1|t-1} = (\hat{x}_{t-1|t-1},\ \hat{x}_{t-1|t-1} + \sqrt{(n+\lambda)\Sigma_{t-1|t-1}},\ \hat{x}_{t-1|t-1} - \sqrt{(n+\lambda)\Sigma_{t-1|t-1}})$

2: $\chi^*{}_{t|t-1} = g(u_t, \chi_{t-1|t-1})$

3: $\hat{x}_{t|t-1} = \sum_{i=0}^{2n} w_m{}^{[i]}\ \chi^{*[i]}{}_{t|t-1}$

4: $\hat{\Sigma}_{t|t-1} = \sum_{i=0}^{2n} w_c{}^{[i]}\ (\hat{\chi}^{*[i]}_{t|t-1} - \hat{x}_{t|t-1})(\hat{\chi}^{*[i]}_{t|t-1} - \hat{x}_{t|t-1})^T + R_t$

5: $\hat{Z}_{t|t-1} = h(\hat{\chi}_{t|t-1})$

6: $\hat{z}_{t|t-1} = \sum_{i=0}^{2n} w_m{}^{[i]}\ \hat{Z}^{*[i]}_{t|t-1}$

7: $S_{t|t-1} = \sum_{i=0}^{2n} w_c{}^{[i]}\ (\hat{Z}^{[i]}_{t|t-1} - \hat{z}_{t|t-1})(\hat{Z}^{[i]}_{t|t-1} - \hat{z}_{t|t-1})^T + Q_t$

8: $\hat{\Sigma}^{x,z}_{t|t-1} = \sum_{i=0}^{2n} w_c{}^{[i]}\ (\hat{\chi}^{[i]}_{t|t-1} - \hat{x}_{t|t-1})(\hat{\chi}^{[i]}_{t|t-1} - \hat{x}_{t|t-1})^T$

9: $K_t = \hat{\Sigma}^{x,z}_{t|t-1}\ S_{t|t-1}{}^{-1}$

10: $\hat{x}_{t|t} = \hat{x}_{t|t-1} + K_t(z_t - \hat{z}_{t|t-1})$

11: $\Sigma_{t|t} = \hat{\Sigma}_{t|t-1} - K_t S_{t|t-1} K_t{}^{-1}$

12: **return** $\hat{x}_{t|t},\ \Sigma_{t|t}$

Figure 3.32: Unscented Kalman Filter algorithm

The matrix Q_t, which represents the covariance of measurement noise, is considered to be constant. Meanwhile, the covariance of process noise, R_t, is treated as a tuning parameter. Proper tuning of the process noise covariance ensures that the filter performs well in terms of the posterior estimate covariance while maintaining a level of responsiveness similar to that of the EKF.

3.6 Driving Cycles

All these simulations are conducted utilizing distinct current profiles extrapolated by different European standard driving cycles. Driving cycles are speed profiles based on statistical data.
The United Nations Economic Commission for Europe (UNECE) has

developed an approval procedure for light-duty vehicles with driving cycles. To be commercialized, vehicles must undergo a series of tests to verify the conformity to standards. The tests are executed in the laboratory and are based on specific driving cycles. The aim of the tests is to verify fuel consumption and polluting emissions. Fuel consumption and emission tests are performed on chassis dynamometers. Driving cycles are produced by different countries, in Europe the cycles used for this purpose are NEDC (New European Driving Cycle), WLTP (Worldwide harmonized Light vehicles Test Procedure), and RDE (Real Driving Emission).

WLTC cycle

The Worldwide Harmonized Light Vehicles Test Procedure (WLTP) comprises a series of protocols developed by the UNECE. Implemented in 2017 to replace the NEDC cycle, which was deemed less realistic, particularly in terms of acceleration values, WLTP mandates various WLTC cycles for emission tests in Europe. These cycles are categorized based on the power-to-mass (PMR) ratio, with three distinct vehicle categories being considered:

- Class 1: low-power vehicles with PMR $\leq$ 22 W/Kg
- Class 2: vehicles with 22 W/Kg $<$ PMR $\leq$ 34 W/Kg
- Class 3: high-power vehicles with PMR $>$ 34 W/Kg

The cycle can be subdivided into four parts of increasing speed, for urban, rural, and highway scenarios:

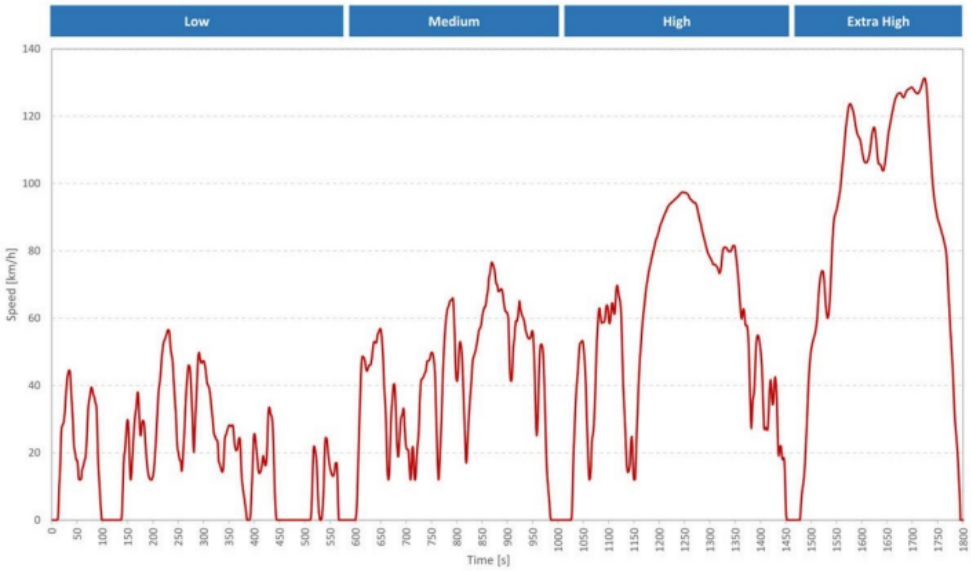

Figure 3.33: WLTP cycle

The cycle parameters are reported in the following table [30]:

Parameter	Low	Medium	High	Extra-high	Total
Distance [km]	3095	4756	7162	8254	23266
Total time [s]	589	433	455	323	1800
Average speed [km/h]	18.9	39.5	56.7	92.0	46.5
Maximum speed [km/h]	56.5	76.6	97.4	131.3	131.3
Maximum acceleration $[m/s^2]$	1.47	1.57	1.58	1.03	1.58

Table 3.3: WLTC parameters

RDE cycle

The Real Driving Emission (RDE) cycles are implemented to assess vehicle emissions in actual driving conditions rather than relying solely on test benches, as is the case with WLTC or NEDC. This cycle encompasses three distinct driving scenarios: urban, rural, and highway. The urban scenario has a maximum speed of 60 km/h, the rural scenario spans speeds between 60 km/h and 90 km/h, while the highway scenario

is designed for speeds above 90 km/h up to 130 km/h. Detailed specifications are provided in the figure 3.34.

Trip specifics		Provision set in the legal text
Total trip duration		Between 90 and 120 min
Distance	Urban	>16 km
	Rural	>16 km
	Motorway	>16 km
Trip composition	Urban	29% to 44% of distance
	Rural	23% to 43% of distance
	Motorway	23% to 43% of distance
Average speeds	Urban	15 to 40 km/h
	Rural	Between 60 and 90 km/h
	Motorway	> 90 km/h (>100 km/h for at least 5 min)

Figure 3.34: RDE specifics [31]

Chapter 4

Simulation and Results

4.1 Model setup

As explained in the chapter 2.6.1 there are different types of lithium batteries. In this thesis work a Lithium Nickel Manganese Cobalt Oxide (NMC) battery was taken into consideration. This cathode pairing stands out as one of the most successful Li-ion systems. Nickel, recognized for its high specific energy, has a drawback of poor stability, while manganese boasts excellent stability but lower specific energy. The amalgamation of these two metals enables compensation for the respective weaknesses of each.
The simulations are all performed considering a battery cell, by performing the same simulations on the entire battery pack the temperature results are similar because we consider the battery modeled as a single block, and by proportionally increasing the values the results are the same. This result can be demonstrated starting from the relationship used in 3.12 to calculate the output temperature T_A.

To calculate the temperature for the battery cell:

$$T_{A,cell} = T_{B,cell} + \frac{R_{cell} I^2}{h A_{cell,exchange}} \tag{4.1}$$

Where the cell parameters are illustrated in 4.1.
To calculate the temperature for the entire battery pack the following formula is used:

$$T_{A,batt} = T_{B,batt} + \frac{R_{batt} I^2}{h A_{batt,exchange}} \tag{4.2}$$

Where the cell parameters are illustrated in 4.3.
From the formulas presented in 4.3 and 4.4, the equations used to determine the battery pack temperature became:

$$T_{A,batt} = T_{B,batt} + \frac{(R_{cell} N_s / N_p)(I N_p)^2}{h(A_{cell,exchange} N s N p)} \tag{4.3}$$

where N_s is the number of battery cells in series N_p is the number of series in parallel in the battery pack and $T_{B,cell} = T_{B,batt}$
By making the necessary simplifications, it is clear that the two expressions are similar. So we can conclude that:

$$\Delta T_{batt} = \Delta T_{cell}$$

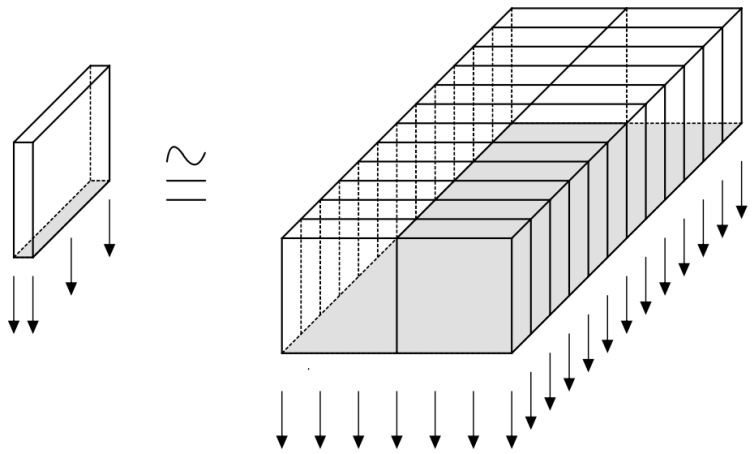

Figure 4.1: Battery cell and Battery pack

Cell parameters

Symbol	Description	Value
$V_{cell_{max}}$	Maximum cell voltage [V]	4.3
$V_{cell_{nom}}$	Nominal cell voltage [V]	3.7
$V_{cell_{min}}$	Minimum cell voltage [V]	2.7
AH	Ampere-hour rating [hrA]	16
R_i	Internal resistance [$m\Omega$]	2
C_p	Thermal capacity [J/KgK]	1200
N_s	Number of cell in series	12
N_p	Modules in parallel	2

Table 4.1: cell parameters

The differences between the various types of batteries are not only in their chemical structure but also in their geometry. The battery cell under analysis is a prismatic battery. The cell dimension for this prismatic lithium-ion NCM battery is illustrated in the table 4.2.

Height [m]	0.12
Length [m]	0.18
Width [m]	0.04
Mass of the cell [Kg]	0.5
Thermal mass [J/K]	600

Table 4.2: cell dimension

For calculating the total area of the battery cell:

$$A_{cell,tot} = 2((Height * Length) + (Height * Width) + (Length * Width))$$

$$A_{cell,tot} = 0.0672m^2$$

For the simulations, not the total area was taken into consideration but only the exchange surface which is equivalent to the lower part of the cell. So:

$$A_{cell,exchange} = Height * Width = 0.0072m^2$$

Thanks to the cell parameters we can calculate battery parameters as follow:

Parameter	Formula	Value
Nominal voltage [V]	$V_{cell_{max}} Ns$	50.4
V_1 [V]	$V_{cell_{nom}} N_s$	44.4
AH [Ahr]	$N_p AH_{cell}$	32
AH_0 [Ahr]	$SOC_0 AH$	19.2
AH_1 [Ahr]	AH/2	16
Battery Capacity [Whr]	$V_1 AH$	1420.80
Internal resistance [$m\Omega$]	$(N_s/N_p)R_{i_{cell}}$	12

Table 4.3: Battery parameters

Battery dimension are illustrated in table 4.4

Parameter	Formula	Value
Height of the battery [m]	Height	0.12
Length of battery [m]	$Length * N_p$	0.18
Width of battery [m]	$Width * N_s$	0.48
Battery mass [Kg]	$M_{cell} * N_s * N_p$	12
Battery thermal mass [J/K]	$Battery\ mass * Thermal\ capacity$	600

Table 4.4: Battery dimension

For calculating the total area of the battery:

$$A_{bat,tot} = 2((Height * Length) + (Height * Width) + (Length * Width))$$

$$A_{bat,tot} = 0.5472m^2$$

For the simulations, as in the previous case, not the total area was considered but only the exchange surface which is equivalent to the lower part of the battery. So:

$$A_{bat,exchange} = A_{cell} N_s N_p = 0.1728m^2$$

4.2 Cooling system design

The goal of incorporating thermal dependence into the battery is to extract parameters for the design of the cooling system.
The assumptions to be considered include that the battery in question exchanges heat with the exchanger through convection in a well-defined area ($A_{cell,exchange}$ and $A_{batt,exchange}$). The area is one of the parameters considered for the design of the cooling system, kept constant.
Other parameters that are useful for the design of the cooling system are the exchange temperature and the heat transfer coefficient. The exchange temperatures used are 25 $°C$ and 30 $°C$ because it is assumed that the cooling temperature is already "hot" because it has already exchanged with the battery and the ambient temperature (about 25 $°C$).
In terms of the heat transfer coefficient, this study considered two values: 20 and 30 $\frac{W}{m^2K}$. The choice of these values was made based on the findings reported in the referenced study [27].

4.3 Results thermal model

The optimal operating temperatures for a lithium-ion battery range from 20$°C$ to 30$°C$, with temperatures between -40 $°C$ and 60$°C$ also permissible. The higher the operating temperature of the cell, the faster

its aging rate. If the temperature becomes excessively high (beyond 80-100°C), the active materials inside the cell can become thermally unstable. Therefore, temperature control is a crucial factor for both battery performance and lifespan.
All these simulations are conducted utilizing distinct current profiles extrapolated by different European standard driving cycles, more precisely, RDE and WLTC.

4.3.1 Simulation of the temperature trend at 1C for constant current and power

To demonstrate that the model in question is sensitive to changes in $T_{exchange}$ and heat transfer coefficient (h), the following simulations take into account two factors:
The heat transfer coefficient (h) was initially tested with different values (h= [5, 15, 30, 50] $\frac{W}{m^2K}$)
The exchange temperatures used are 30 °C and 40 °C.
The initial simulations are conducted with both constant current input and constant power input.

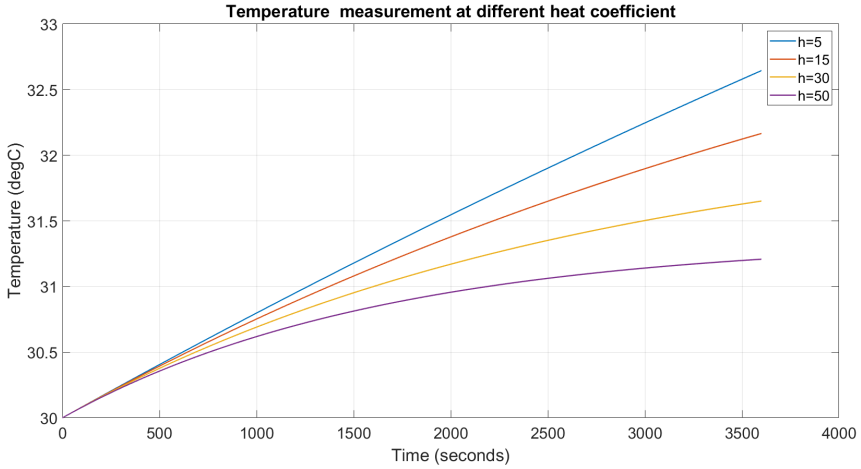

Figure 4.2: Temperature measurement at different heat coefficient with constant current as input

In figure 4.2 the exchange temperature taken into consideration is 30 $°C$ and the temperature values measured for each heat transfer coefficient (h) are reported in the table 4.5. A discharge current equal to 1C was applied and simulated for 3600 seconds.

h $[\frac{W}{m^2K}]$	T_{max} $[°C]$
5	32.6
15	32.2
30	31.7
50	31.21

Table 4.5: T_{max} at different h at T_{exch} =30 $°C$ with constant current

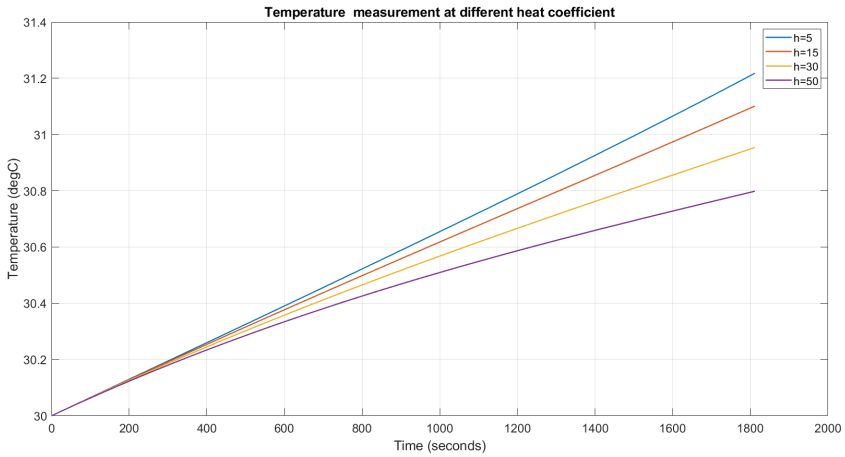

Figure 4.3: Temperature measurement at different heat coefficient with constant power as input

In figure 4.3 the same consideration is taken into account with the only difference being that a constant power input is used, which is divided by the voltage measured by a voltage sensor connected in parallel to the battery. The temperature values measured for each heat transfer coefficient (h) are shown in the table 4.6:

h $[\frac{W}{m^2K}]$	T_{max} $[°C]$
5	31.7
15	31.43
30	31.09
50	30.80

Table 4.6: T_{max} at different h at T_{exch} =30 $°C$ with constant power

The same simulations were performed by varying the value of the exchange temperature and using 40 $°C$.

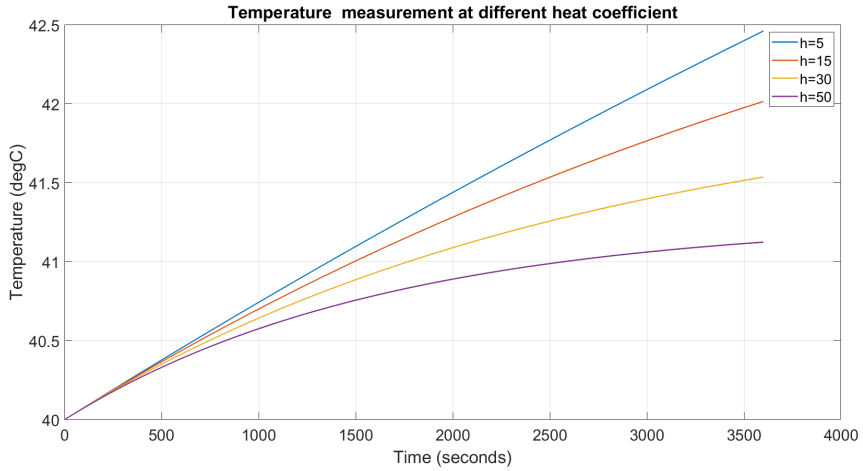

Figure 4.4: Temperature measurement at different heat coefficient with constant current as input

The measured temperature, in this case, are in table 4.7 :

h $[\frac{W}{m^2K}]$	T_{max} $[°C]$
5	42.5
15	42
30	41.54
50	41.12

Table 4.7: T_{max} at different h at T_{exch} =40 $°C$ with constant current

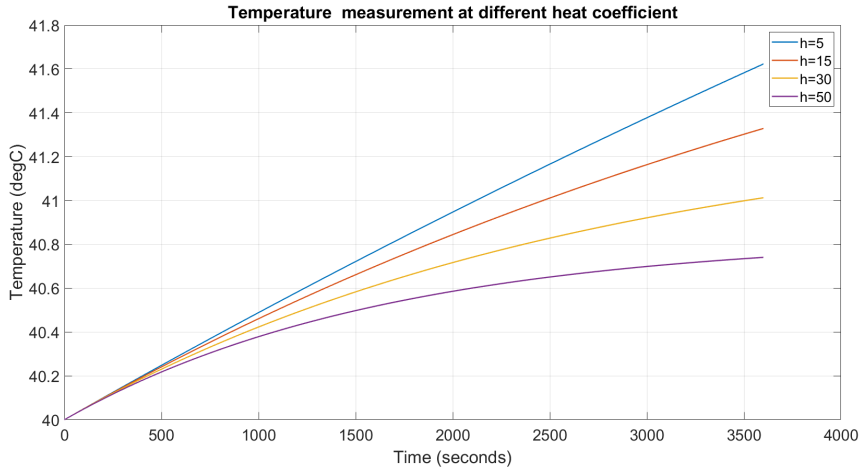

Figure 4.5: Temperature measurement at different heat coefficient with constant power as input

The temperature values measured for each heat transfer coefficient (h) are illustrated in the table 4.8

h $[\frac{W}{m^2K}]$	T_{max} $[°C]$
5	41.6
15	41.33
30	41.01
50	40.74

Table 4.8: T_{max} at different h at T_{exch} =40 $°C$ with constant power

From these simulations, we can infer that the temperature increases linearly, and the temperature difference (ΔT) between the smallest and largest heat transfer coefficients is approximately 1-1.5 $°C$.

From these simulations, we observe that indeed, the analyzed model is sensitive to variations in these two parameters.
Furthermore, as explained in the chapter 3.4.1, when the surrounding temperature is around 30 $°C$, a minimum heat transfer coefficient of 15 $\frac{W}{m^2K}$ is required.

4.3.2 Simulation of the power profile for the WLTC cycle

In these simulations, the power profile is obtained from a WLTC cycle. Below are the current, voltage, power, and SOC characteristics.

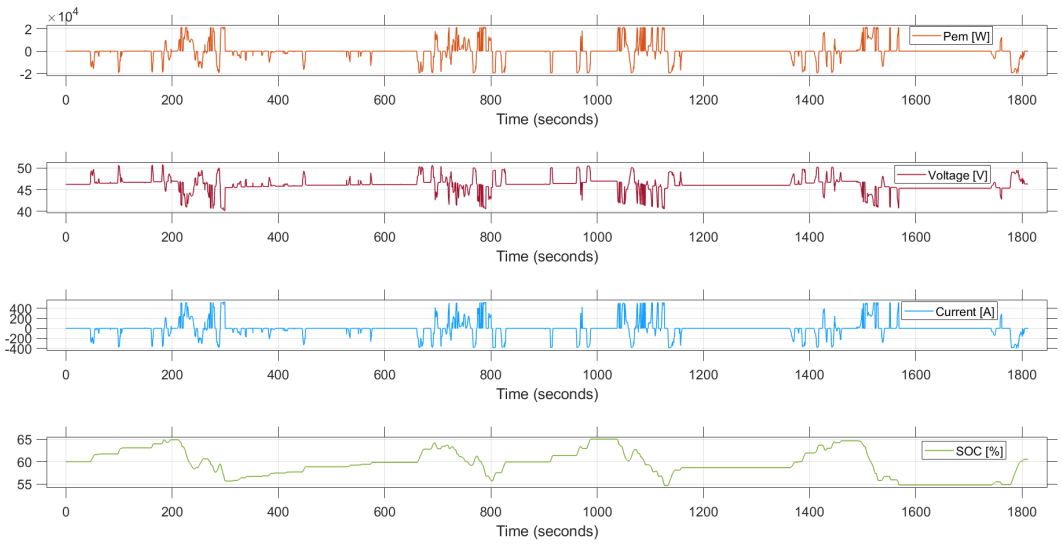

Figure 4.6: WLTC profile in the battery pack

Since the goal is to find optimal parameters to ensure that the battery operates within a specific temperature range for designing a cooling system, the combinations of h and $T_{exchange}$ studied in these simulations are four:

h $[\frac{W}{m^2K}]$	$T_{exchange}$ $[°C]$
20	25
30	25
20	30
30	30

Table 4.9: combinations of h and $T_{exchange}$

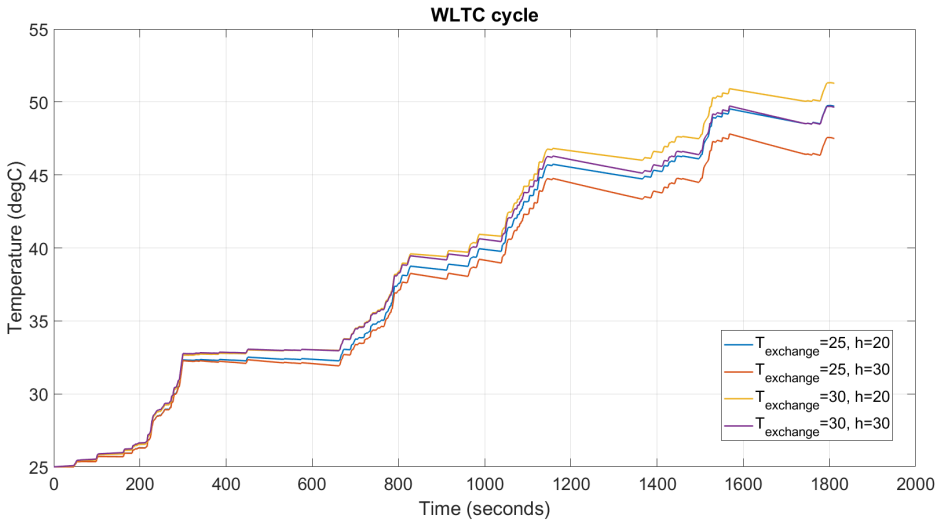

Figure 4.7: Temperature measurement for WLTC cycle in the battery pack

It can be observed that in all combinations, the temperature reached by this cycle hovers around 50 $°C$ and the one that appears optimal is the one with $T_{exchange} = 25$ and $h = 30$. This temperature result is not optimal but certainly still acceptable. This result is achieved because, as can be seen in the figure 4.6, there is a high torque demand fulfilled by the electric motor.
The efficiency map of the electric motor shown in figure 4.8, can observe

the operating points of the WLTC. The trends in the map can also reflect the battery's working zone showing its utilization during the cycle, indicating energy discharge or recharging. Indeed, from this map, it can be observed that in this cycle, the operation frequently occurs at high efficiency and involves high torque demand.

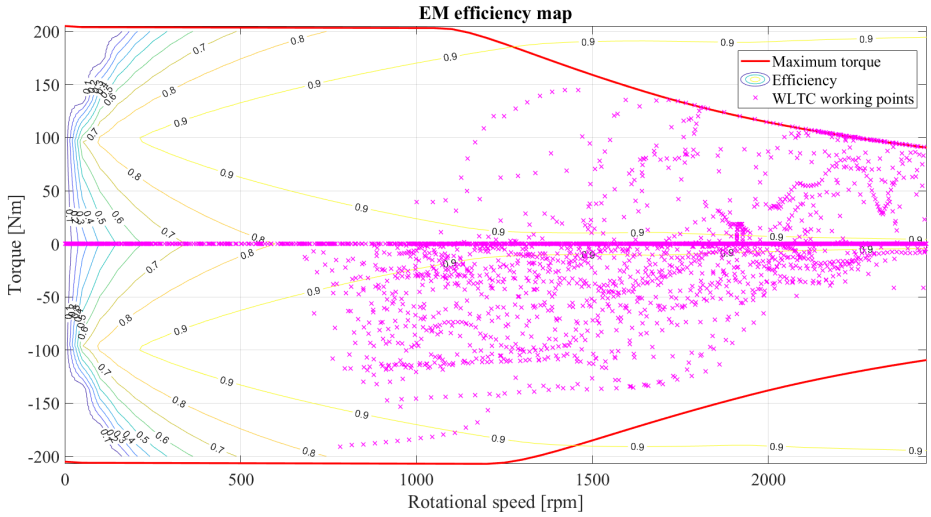

Figure 4.8: EM efficiency map of WLTC

4.3.3 Simulation of the power profile for the RDE cycle

In these simulations, the current profile is provided from an RDE cycle. As mentioned in 3.6, this cycle comprises three different driving scenarios: urban, rural, and highway. In the urban setting, the maximum speed is capped at 60 km/h. The rural scenario encompasses speeds ranging from 60 km/h to 90 km/h, while the highway scenario is tailored for speeds exceeding 90 km/h and reaching up to 130 km/h.
The first analyzed case is the RDE urban, which exhibits the following characteristics of current, voltage, power, and State of Charge (SOC):

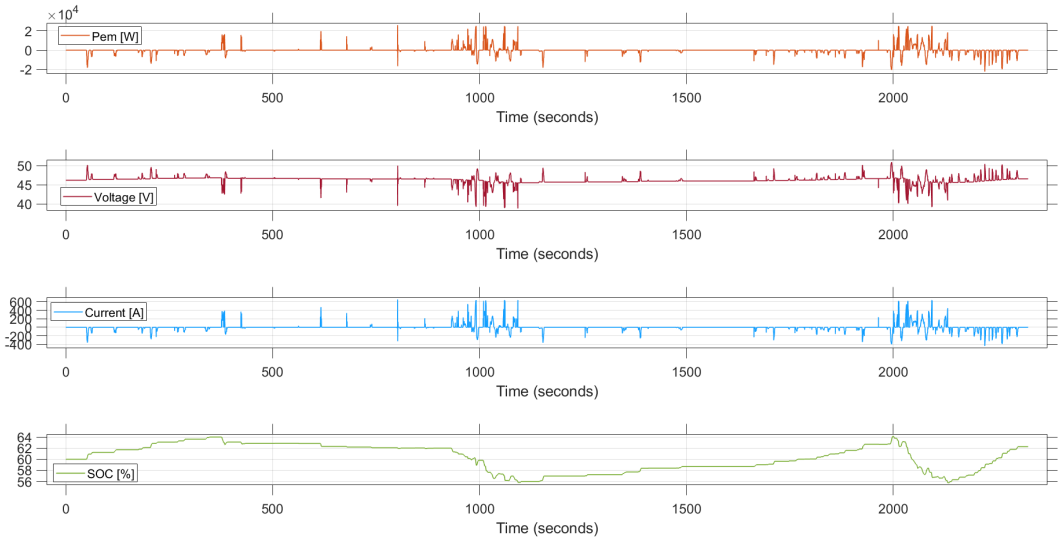

Figure 4.9: RDE urban profile in the battery pack

Also for this cycle, combinations are considered in the table 4.9.

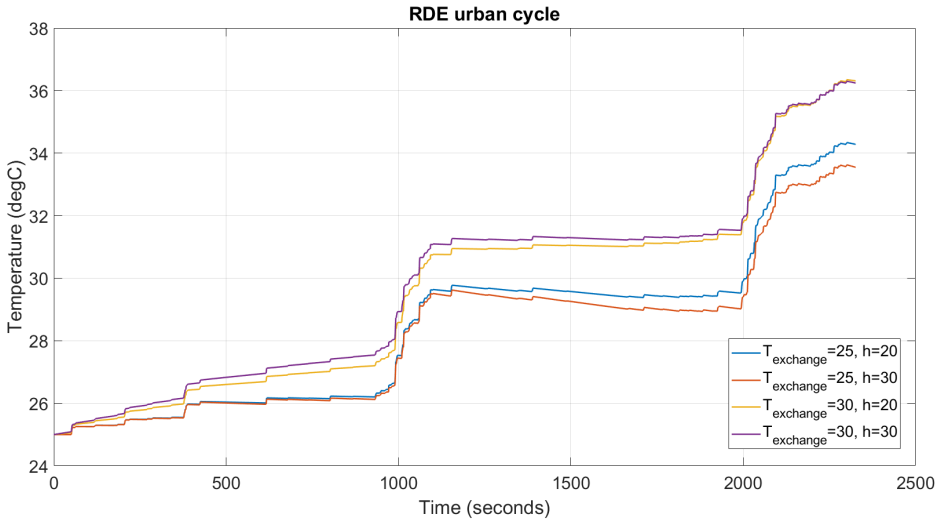

Figure 4.10: Temperature measurement for RDE urban cycle in the battery pack

In contrast to the previous cycle, in this case, the temperatures measured are lower, around $35°C$. This is because, as it is shown in Figure 4.11, the urban RDE operates at low speeds, resulting in a

lower demand for torque from the electric motor so the temperatures registered are not high.

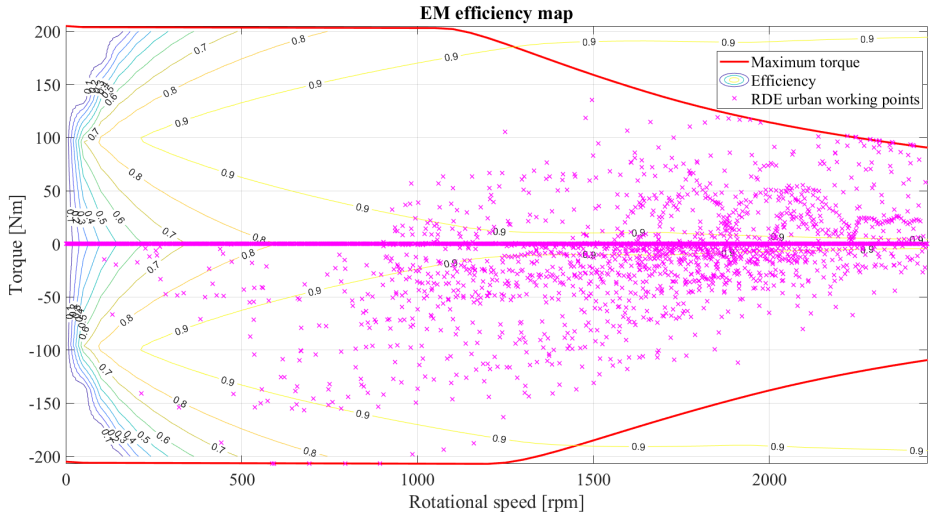

Figure 4.11: EM efficiency map of RDE urban

The second analyzed case is the RDE rural, and all its characteristics are presented in the figure below:

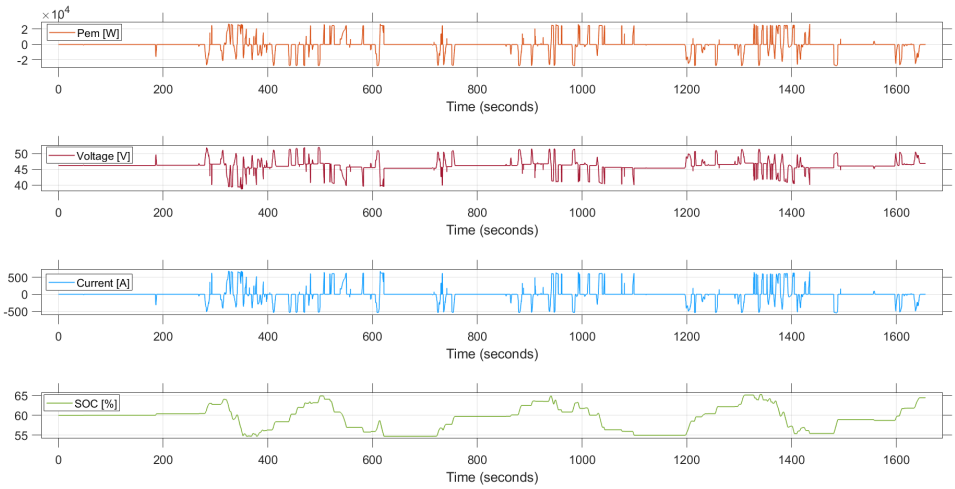

Figure 4.12: RDE rural profile in the battery pack

Here too, the same assumptions are taken into account.

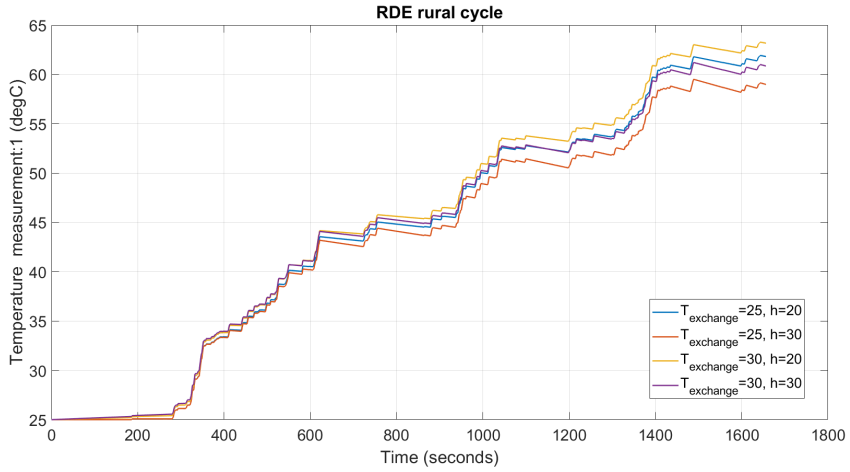

Figure 4.13: Temperature measurement for RDE rural cycle in the battery pack

In this scenario, it operates at much higher speeds, causing significant stress on the battery and resulting in elevated temperatures. This behavior is clearly illustrated in the figure 4.14. This continuous demand for current from the battery leads to reaching 63 $°C$ in the worst case possible.

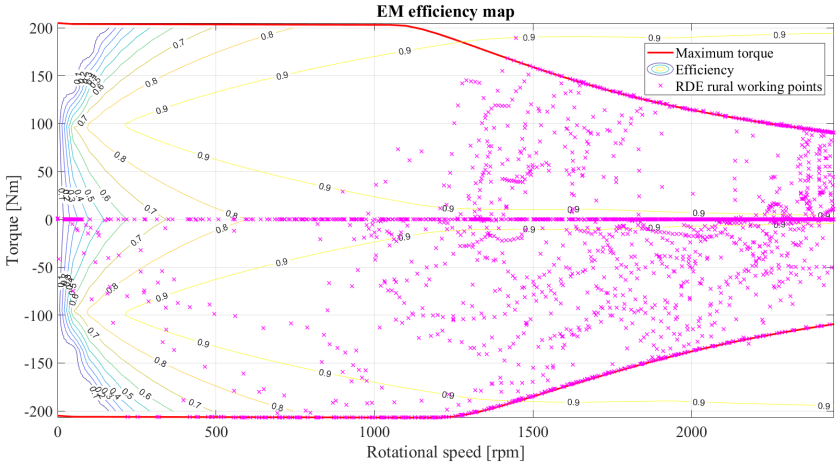

Figure 4.14: EM efficiency map of RDE rural

The analysis of the RDE motorway cycle proves to be interesting. The characteristics of current, voltage, power, and State of Charge (SOC) are illustrated in the figure below:

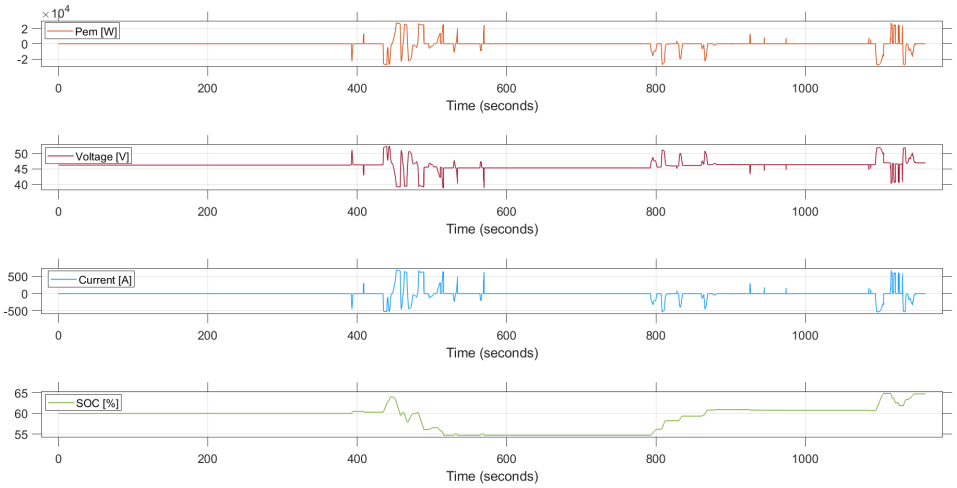

Figure 4.15: RDE motorway profile in the battery pack

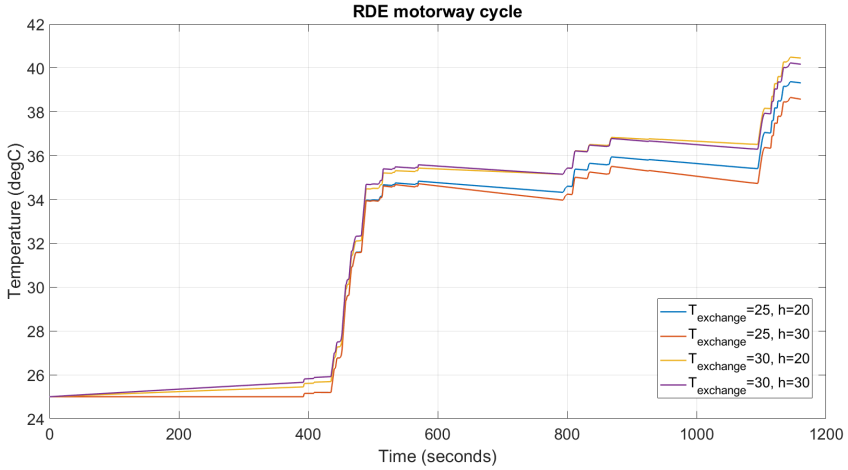

Figure 4.16: Temperature measurement for RDE motorway cycle in the battery pack

This case is intriguing because, as evident from Figure 4.15, there are frequent instances of zero power. This occurs because, being a

cycle that operates at very high speeds, the torque demand is so high that the electric motor cannot meet it, and it is only satisfied by the internal combustion engine (ICE). This also explains that when the torque is satisfied, the battery is highly stressed, leading to quite high temperatures approximately equal to 40 $°C$.
It is also evident from the figure 4.17, depicting the operating points of the electric motor. It is observed that there are significantly fewer points compared to the other maps previously analyzed, and the few that exist operate at very high speeds and torque. Therefore, as mentioned earlier, even though the internal combustion engine (ICE) predominantly operates in this cycle, the battery undergoes degradation due to the high current demand.

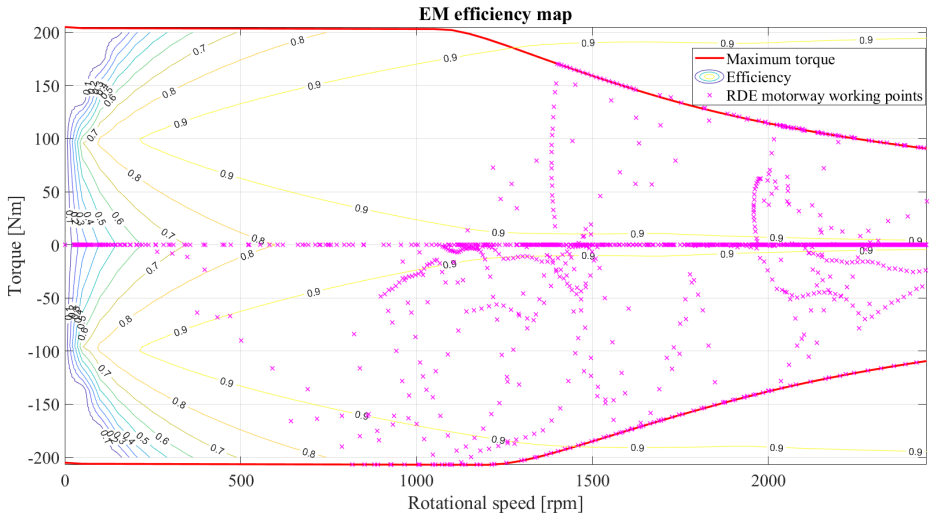

Figure 4.17: EM efficiency map of RDE motorway

In conclusion, the analysis of the thermal behavior of the battery concerning the complete RDE is presented, providing a comprehensive overview of the entire driving cycle. The characteristics of current, voltage, power, and state of charge are depicted in the figure below in figure 4.18.

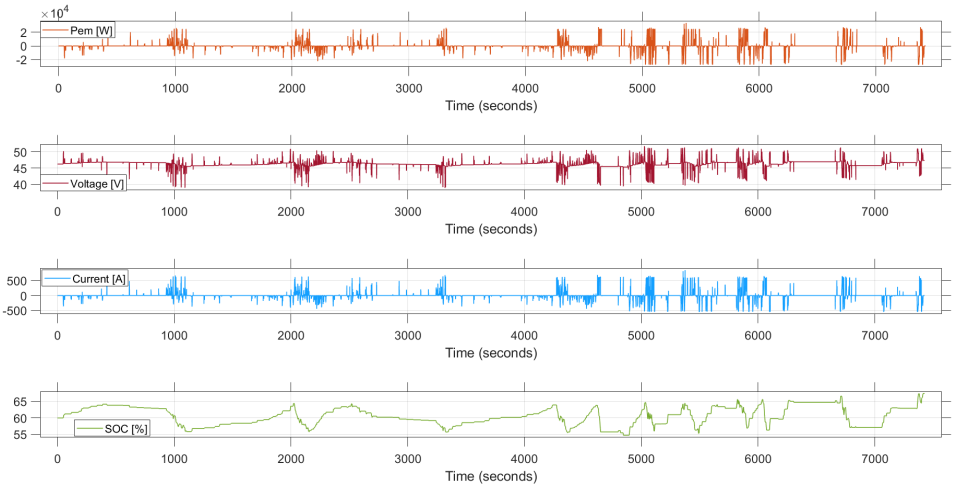

Figure 4.18: RDE profile in the battery pack

The same assumptions are taken into account and also in this case the optimal combination results the one with $T_{exchange}$ =25 $°C$ and h=30 $\frac{W}{m^2K}$.

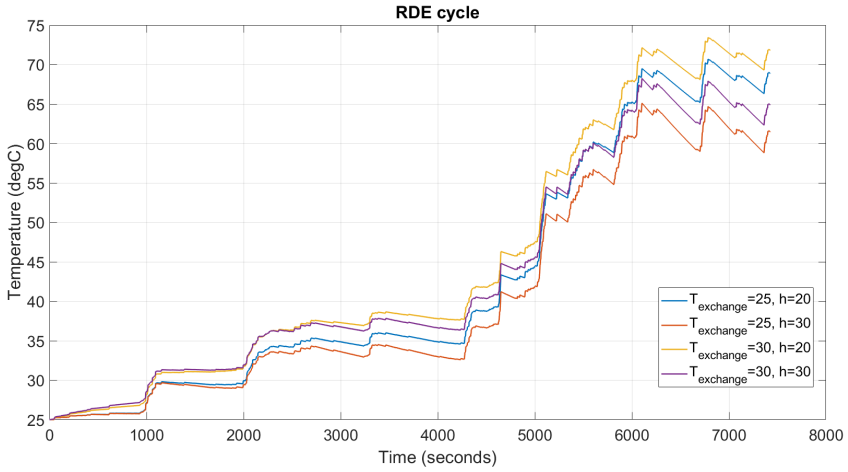

Figure 4.19: Temperature measurement for RDE cycle in the battery pack

Here, all the considerations made for the various RDE cycles hold true.

It is clear that in RDE complete the measured temperatures are too high. The solution can be integrating the temperature parameter into the control logic to limit the electric machine power, which serves to safeguard the battery from deterioration.

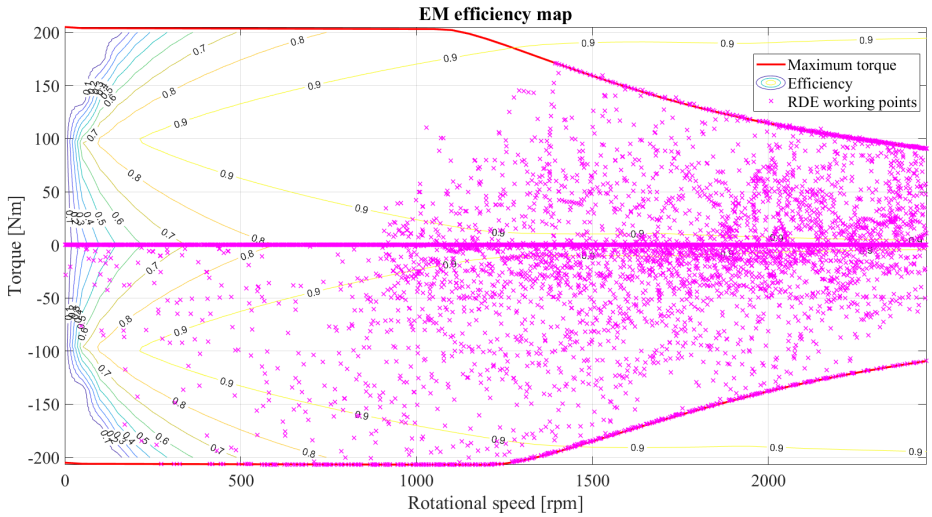

Figure 4.20: EM efficiency map for RDE complete

From this efficiency map of the electric motor, encompassing all operating points of a complete RDE cycle, one can observe the extent to which the battery is stressed.

For completeness, here in figure 4.21 is the efficiency map comparison graph that contrasts both cycles used in the simulations:

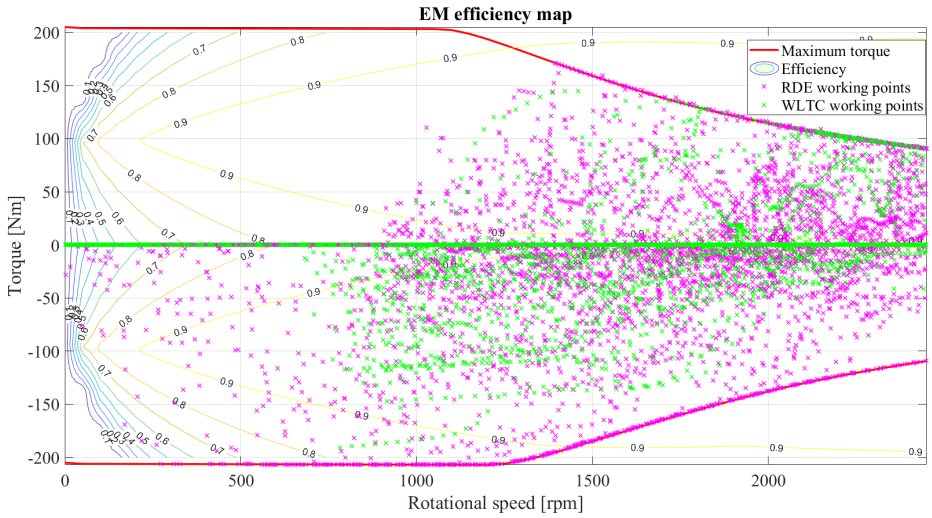

Figure 4.21: EM efficiency map

From this map, it is evident that both cycles operate at high efficiency but the RDE operates more under high torque demands. Thus, in the RDE cycle, the battery undergoes more degradation compared to the WLTC cycle.

4.4 Kalman filter tuning

As explained in Chapter 3.5.1, in the Unscendent Kalman Filter, the distribution is represented by a set of strategically selected sample points, known as σ-points. To compute these σ-points and their corresponding weights, three parameters need to be defined:

- $\alpha = 1$; It is a coefficient that controls the dispersion of σ-points. It is within the range $0 < \alpha \leq 1$.
- $\beta = 2$; For a Gaussian distribution, the optimal value in this case is set to 2.
- $k = 3 - n = 0$; n indicates the number of states, which, in this case, are three: State of Charge (SOC), voltage, and internal resistance (R_0).

From the algorithm illustrated in figure 3.32, it can be noted that three other parameters are crucial to set:

- Q_t that represents the process noise covariance. Presuming a very small process variance, we let $Q_t = \epsilon I$, where ϵ is a small positive value. It is possible to set ϵ to zero, but assuming a small but non-zero value provides more flexibility in 'tuning' the filter [32].

$$Q_t = \begin{bmatrix} 1e-14 & 0 & 0 \\ 0 & 1e-14 & 0 \\ 0 & 0 & 1e-14 \end{bmatrix}$$

- $R_t = 0.75$ that represents measurements noise covariance. A high R_t-value implies that the filter anticipates a significant amount of noise in the measurements. Since the system has only one input variable (the current), the measurement noise is a one-element vector.

- P_0 that represents the initial state error covariance. During the initial state of a system, the error covariance is represented by P0. As the initial state at time step 0 is 0, P_0 is set to small values to describe the initial state. In the beginning, small Kalman gains will be obtained, and as P_0 increases due to noise (determined by the covariance matrix Q_t), the Kalman gains will gradually increase.

$$P_0 = \begin{bmatrix} 1e-12 & 0 & 0 \\ 0 & 1e-12 & 0 \\ 0 & 0 & 1e-12 \end{bmatrix}$$

Other input parameters to the filter include the initial state of charge, set at 60% according to the strategy used in the model, and the internal resistance value equal to that reported in the battery datasheet, i.e., 12 $m\Omega$.

As input for the filter is added a noise for both current and voltage as illustrated in the following figure:

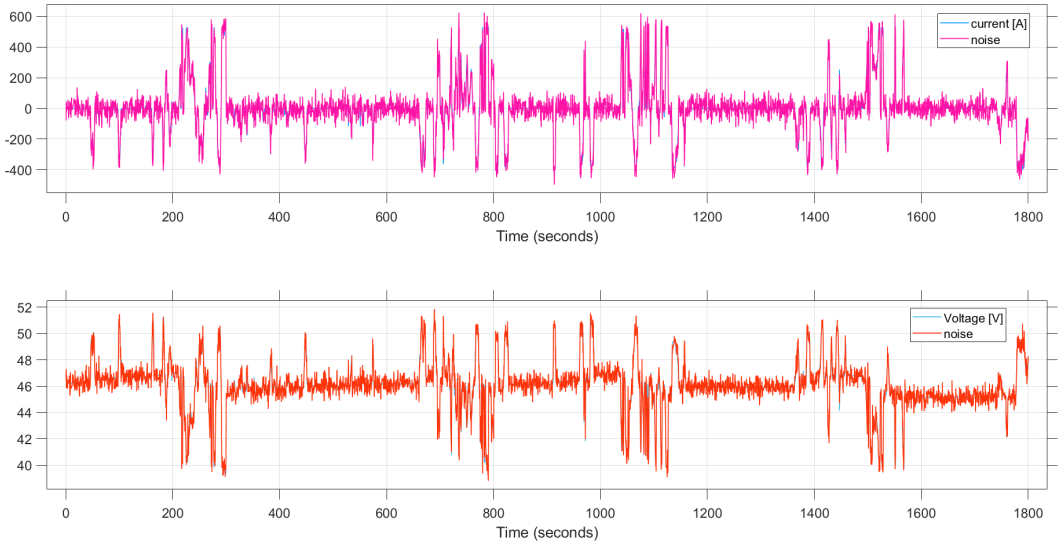

Figure 4.22: Current and voltage with noise

4.4.1 Estimation of SOC, R, and SOH in WLTC cycle

The simulation depicted in figure 4.23 was conducted using a power profile extracted from a WLTC cycle and setting the exchange temperature to 25 $°C$

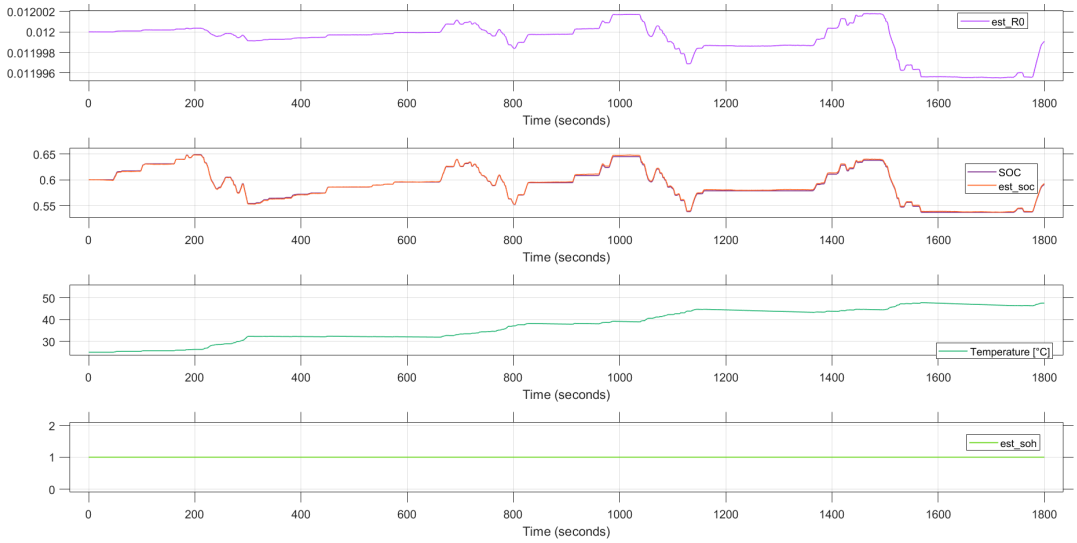

Figure 4.23: Estimation of SOC, R, and SOH in WLTC cycle

From this simulation, it is possible to conclude that the estimated State of Charge (SOC) overlaps with the actual one, indicating optimal estimation. Regarding the internal resistance, we observe that its value decreases slowly due to deterioration. Lastly, the State of Health (SOH) estimation remains at 100% because the battery is being tested for a duration of 1800 seconds (30 minutes), so it is normal for the SOH to be at its maximum.
Based on findings from a study [33] that examined the estimation of battery state of health and state of charge, the following can be confirmed: if the State-of-Health remains constant at 100%, and the State-of-Charge varies only slightly within the 50% to 70% range, then the internal resistance of the battery tends to decrease. This behavior is depicted in figure 4.24 where the dependency of internal resistance on SOC and SOH is illustrated in a 3D graph.

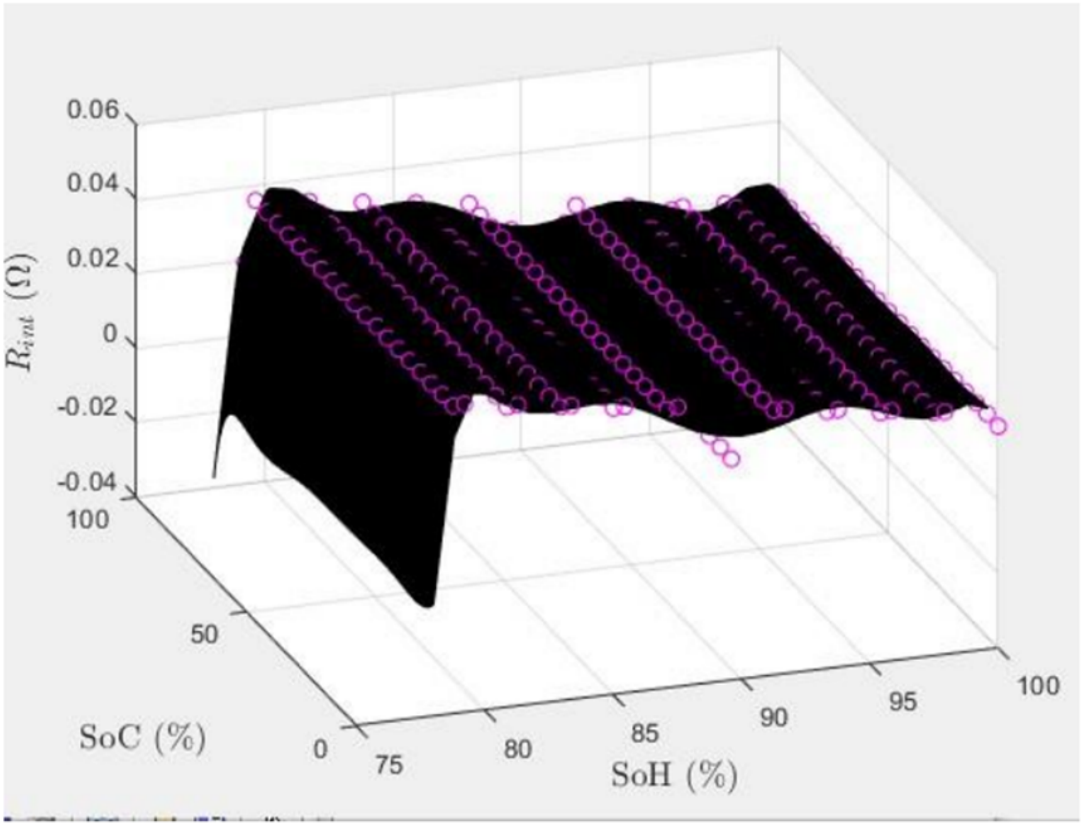

Figure 4.24: Dependency of internal resistance on SOC and SOH [33]

4.4.2 Estimation of SOC, R, and SOH in RDE cycle

These simulations were conducted using a power profile extracted from an complete RDE cycle and setting the exchange temperature to 25 $^{\circ}C$.

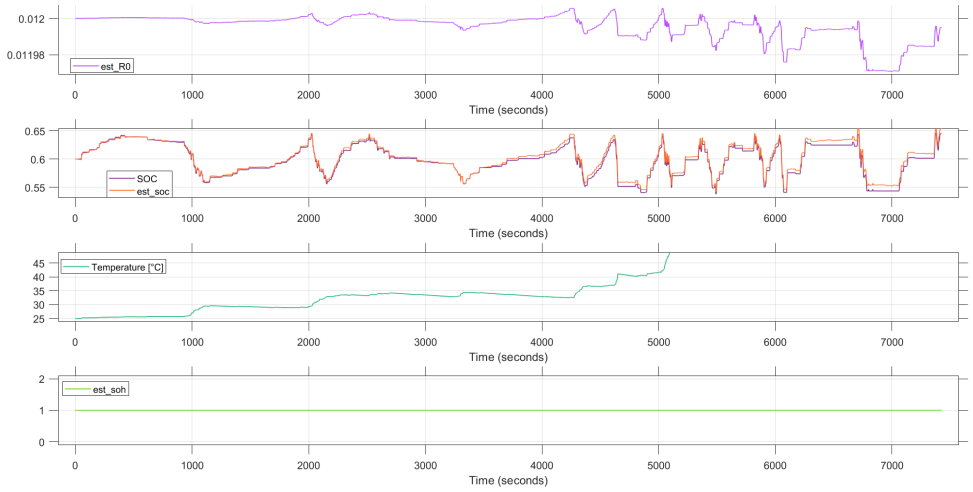

Figure 4.25: Estimation of SOC, R, and SOH in RDE cycle

Here the same considerations as previous cycle are valid. The only difference is that the temperature is higher as explained before. This leads to a worse deterioration of the internal resistance.

4.4.3 Simulation of a modified WLTC cycle

The same simulation was conducted by alternating the previously used WLTC cycle with profiles of zero power (thus, current equal to zero) of the same duration as the cycle (30 minutes).

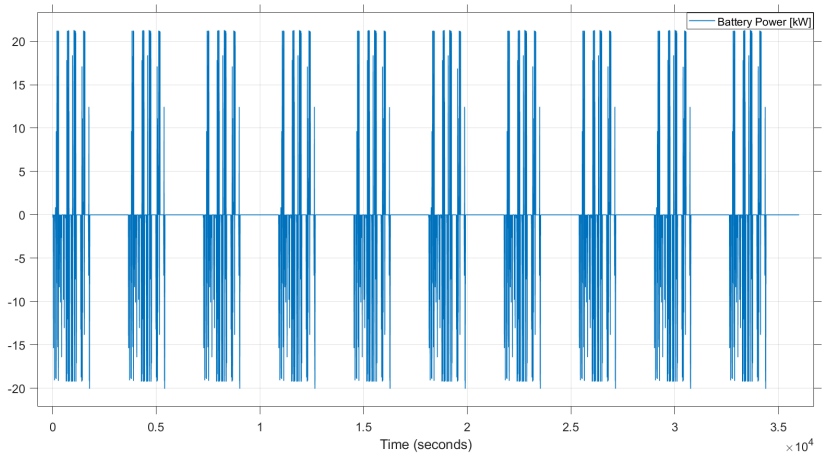

Figure 4.26: New power profile

For the assessment of the SOH and the filter performance in the long term, a new current profile obtained by concatenating the previously used WLTC cycle with zero power vectors was tested.

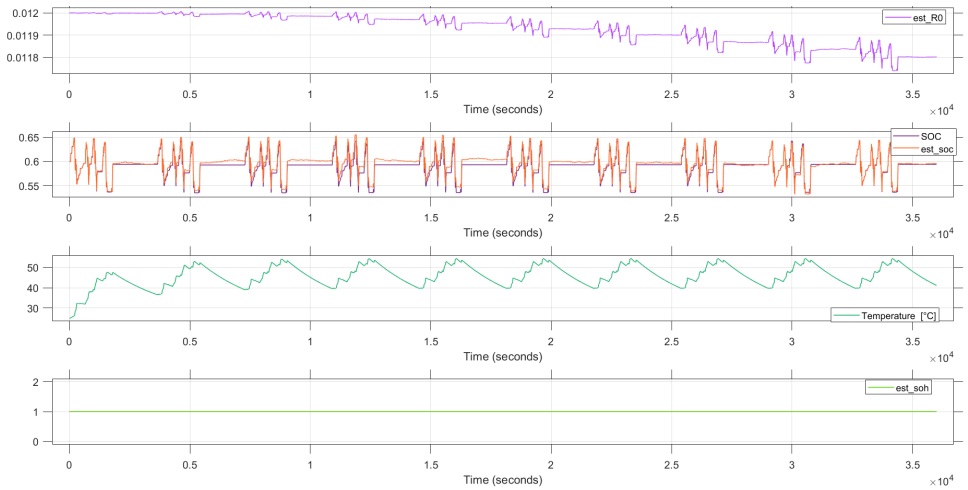

Figure 4.27: Estimation of SOC,R and SOH

From these simulations, it is possible to conclude that the estimated SOC closely follows the real value, considering noisy measurements of voltage and current, thus being promising for real application. Regarding the internal resistance, it is observed that its value decreases slowly

due to deterioration and the increase of temperature. Lastly, the SOH estimation remains at 100% because the battery is being tested for 10 hours maximum so this value is expected to remain stable with the power profiles considered.

Chapter 5

Conclusion

This concluding chapter aims to recapitulate the objectives set for this project, outline the methodologies employed, and present the ultimate results obtained for each task, while also exploring potential avenues for future enhancements.
The primary goal of this thesis is to improve the Energy Management Strategy of a Hybrid Electric Vehicle with regard to battery thermal behavior and state of health. To achieve this, two distinct approaches are analyzed. The first investigates the feasibility of a Hybrid Energy Storage System (HESS) incorporating a supercapacitor parallel to the main battery. The second approach aims to enhance the Energy Management System (EMS) by considering battery thermal behavior and implementing State-of-Charge, internal resistance, and State-of-Health estimation.
The study begins by employing a forward model of a 48V P1 hybrid light-duty commercial vehicle in Matlab Simulink, introducing and analyzing the supercapacitor's model and performance. The results of this analysis show that the supercapacitor does not enhance the efficiency of Energy Storage Systems (ESS) in the context of the 48V P1 architecture. Furthermore, as it is explained in the chapter 2.4.3, the main problem of HESS architecture in which a battery and supercapacitor are in parallel is that the power shared between them is determined by their respective series resistances. To prevent this phenomenon, a converter was installed between the two ESS. Unfortunately, adding a

DC/DC converter increases the cost and weight of the entire system and reduces its efficiency. So, it can be concluded that, in the analyzed case study, it is not a viable strategy to implement for improving the Energy Management System (EMS).
The second analysis consists of a new battery model in which thermal dynamics and cooling are incorporated. Temperature control is crucial for battery performance and lifespan. The objective of introducing thermal dependence into the battery is to derive parameters for cooling system design. Assumptions include heat exchange between the battery and air through convection in defined areas ($A_{cell,exchange}$ and $A_{batt,exchange}$), this is considered a constant parameter for cooling system design. Additional parameters studied to obtain the cooling system design include the exchange temperatures and heat transfer coefficient. For the first parameter $25°C$ and $30°C$ are the examined values, and for the heat transfer coefficient, two values (20 and 30 $\frac{W}{m^2K}$) are considered. Simulations use distinct current profiles extracted from different European standard driving cycles, specifically RDE and WLTC.
It can be observed that in the WLTC cycle, the temperature reached hovers around 50 $°C$. This temperature result is not optimal but certainly still acceptable. Similarly, in the case of the RDE urban and motorway cycles, the temperature operates within an acceptable range. In the urban scenario, this is attributed to working at lower temperatures, while in the motorway scenario, there are frequent instances of zero power. This occurs because, being a cycle that operates at very high speeds, the torque demand is so high that the electric motor cannot meet it, and it is only satisfied by the internal combustion engine (ICE). On the other hand, the RDE rural operates at much higher speeds, causing significant stress on the battery and resulting in elevated temperatures. The solution can be integrating the temperature parameter into the control logic to limit the electric machine power, which serves to safeguard the battery from deterioration.
To optimize battery usage, the tuning of a Kalman filter was performed to obtain the SOC and internal resistance estimation. These parameters are useful to calculate the State of Health of the battery. The simulations are executed with the same driving cycles as the previous

model to better understand how the filter works. For the assessment of the SOH and the filter performance in the long term, a new current profile obtained by concatenating the previously used WLTC cycle with zero power vectors was tested. From these simulations, it is possible to conclude that the estimated SOC closely follows the real value, considering noisy measurements of voltage and current, thus being promising for real application. Regarding the internal resistance, it is observed that its value decreases slowly due to deterioration and the increase of temperature. Lastly, the SOH estimation remains at 100% because the battery is being tested for 10 hours maximum so this value is expected to remain stable with the power profiles considered.

5.1 Future works

Future research explores integrating the temperature parameter into the control logic, thus implementing an adaptive ECMS to limit the electric machine power, which serves to safeguard the battery from deterioration. Another possible future work can be the validation of the results by testing a single cell of a battery on a test bench.

Bibliography

[1] *EEA report confirms: electric cars are better for climate and air quality.* URL: https://www.eea.europa.eu/highlights/eea-report-confirms-electric-cars (cit. on p. 1).

[2] *CO2 emissions from cars: facts and figures.* URL: https://www.europarl.europa.eu/news/en/headlines/society/20190313ST031218/co2-emissions-from-cars-facts-and-figures-infographics (cit. on p. 2).

[3] *Transport and environment report 2021 Decarbonising road transport — the role of vehicles, fuels and transport demand.* URL: https://www.eea.europa.eu/publications/transport-and-environment-report-2021 (cit. on p. 3).

[4] *Electric Vehicles.* URL: https://www.iea.org/energy-system/transport/electric-vehicles (cit. on p. 3).

[5] Qicheng Xue Xin Zhang Teng Teng Jibao Zhang Zhiyuan Feng and Qinyang Lv. «A Comprehensive Review on Classification, Energy Management Strategy, and Control Algorithm for Hybrid Electric Vehicles». In: *Energies* (2020) (cit. on pp. 9, 10).

[6] Wenlong Jing, Chean Hung Lai, Wallace S. H. Wong, and M. L. Dennis Wong. «Battery-supercapacitor hybrid energy storage system in standalone DC microgrids: a review». English. In: *IET Renewable Power Generation* 11.4 (Mar. 2017), pp. 461–469. ISSN: 1752-1416. DOI: 10.1049/iet-rpg.2016.0500 (cit. on pp. 12, 15, 29).

[7] A. Ostadi Student Member IEEE M. Kazerani Senior Member IEEE and Shih-Ken Chen. «Hybrid Energy Storage System (HESS) in Vehicular Applications: A Review on Interfacing Battery and Ultra-capacitor Units». In: *IEE* (2013) (cit. on pp. 12, 14, 16).

[8] Xiang Changle, Wang Yanzi, Hu Sideng, and Wang Weida. «A New Topology and Control Strategy for a Hybrid Battery-Ultracapacitor Energy Storage System». In: *Energies* 7.5 (2014), pp. 2874–2896 (cit. on p. 13).

[9] Ziyou Song, Jianqiu Li, Jun Hou, Heath Hofmann, Minggao Ouyang, and Jiuyu Du. «The battery-supercapacitor hybrid energy storage system in electric vehicle applications: A case study». In: *Energy* 154.C (2018), pp. 433–441. DOI: 10.1016/j.energy.2018.04.. URL: https://ideas.repec.org/a/eee/energy/v154y2018icp433-441.html (cit. on p. 15).

[10] Donato Molteni. «Studio e progetto di un convertitore DC/DC per la gestione di supercap su veicoli elettrici». MA thesis. Milano: Politecnico di Milano, 2010 (cit. on p. 18).

[11] Pankaj Saha and Munmun Khanra. «Equivalent Circuit Model of Supercapacitor for Self-Discharge Analysis - A Comparitive Study». In: Oct. 2016. DOI: 10.1109/SCOPES.2016.7955667 (cit. on p. 19).

[12] Mustafa Şahin, F. Blaabjerg, and Ariya Sangwongwanich. «Modelling of Supercapacitors Based on Simplified Equivalent Circuit (CPSS Transactions on Power Electronics and Applications)». In: 6 (Mar. 2021). DOI: 10.24295/CPSSTPEA.2021.00003 (cit. on pp. 19, 20, 49).

[13] Low Wen Yao, Junaidi Abdul Aziz, Pui Yee Kong, and Nik Rumzi Nik Idris. «Modeling of lithium-ion battery using MATLAB/simulink». In: *IECON 2013 - 39th Annual Conference of the IEEE Industrial Electronics Society* (2013), pp. 1729–1734. URL: https://api.semanticscholar.org/CorpusID:28691595 (cit. on p. 22).

[14] Battery University. «BU-402: What Is C-rate?» In: (). URL: https://batteryuniversity.com/article/bu-402-what-is-c-rate (cit. on pp. 23, 24).

[15] Cheng Zhang, Kang Li, Sean Mcloone, and Zhile Yang. «Battery modelling methods for electric vehicles - A review». In: June 2014, pp. 2673–2678. ISBN: 978-3-9524269-1-3. DOI: 10.1109/ECC.2014.6862541 (cit. on pp. 25, 44).

[16] Rui Xiong, Huan Chen, Chun Wang, and Fengchun Sun. «Towards a smarter hybrid energy storage system based on battery and ultracapacitor - A critical review on topology and energy management». In: *Journal of Cleaner Production* 202 (Aug. 2018). DOI: 10.1016/j.jclepro.2018.08.134 (cit. on p. 30).

[17] Simona Onori Lorenzo Serrao Giorgio Rizzoni. *Hybrid Electric Vehicles Energy Management Strategies*. Springer, 2016 (cit. on p. 31).

[18] P. Pettersson, B. Jacobson, F. Bruzelius, P. Johannesson, and L. Fast. «Intrinsic differences between backward and forward vehicle simulation models». In: *IFAC-PapersOnLine* 53.2 (2020). 21st IFAC World Congress, pp. 14292–14299. ISSN: 2405-8963. DOI: https://doi.org/10.1016/j.ifacol.2020.12.1368. URL: https://www.sciencedirect.com/science/article/pii/S2405896320317754 (cit. on p. 34).

[19] Gao Diju, Wei Zhang, Aidi Shen, and Yide Wang. «Parameter Design and Energy Control of the Power Train in a Hybrid Electric Boat». In: *Energies* 10 (July 2017), pp. 1–12. DOI: 10.3390/en10071028 (cit. on p. 43).

[20] S. Barcellona, S. Grillo, and L. Piegari. «A simple battery model for EV range prediction: Theory and experimental validation». In: *2016 International Conference on Electrical Systems for Aircraft, Railway, Ship Propulsion and Road Vehicles International Transportation Electrification Conference (ESARS-ITEC)*. 2016, pp. 1–7. DOI: 10.1109/ESARS-ITEC.2016.7841441 (cit. on pp. 45–49).

[21] Lei Zhang, Xiaosong Hu, Zhenpo Wang, Fengchun Sun, and David G. Dorrell. «A review of supercapacitor modeling, estimation, and applications: A control/management perspective». In: *Renewable and Sustainable Energy Reviews* 81 (2018), pp. 1868–1878. ISSN: 1364-0321. DOI: https://doi.org/10.1016/j.rser.2017.05.283. URL: https://www.sciencedirect.com/science/article/pii/S1364032117309292 (cit. on p. 49).

[22] Vincenzo Musolino, Luigi Piegari, and Enrico Tironi. «New Full-Frequency-Range Supercapacitor Model With Easy Identification Procedure». In: *IEEE Transactions on Industrial Electronics* 60 (Jan. 2013), pp. 112–120. DOI: 10.1109/TIE.2012.2187412 (cit. on p. 52).

[23] Lisheng Shi and M.L. Crow. «Comparison of ultracapacitor electric circuit models». In: Aug. 2008, pp. 1–6. DOI: 10.1109/PES.2008.4596576 (cit. on p. 53).

[24] Mohsen Akbarzadeh, Theodoros Kalogiannis, Joris Jaguemont, Jiacheng He, Lu Jin, Maitane Berecibar, and Joeri Van Mierlo. «Thermal modeling of a high-energy prismatic lithium-ion battery cell and module based on a new thermal characterization methodology». In: *Journal of Energy Storage* 32 (2020), p. 101707. ISSN: 2352-152X. DOI: https://doi.org/10.1016/j.est.2020.101707. URL: https://www.sciencedirect.com/science/article/pii/S2352152X20315449 (cit. on p. 54).

[25] Said Madaoui, Jean-Michel Vinassa, Jocelyn Sabatier, and Franck Guillemard. «An Electrothermal Model of an NMC Lithium-Ion Prismatic Battery Cell for Temperature Distribution Assessment». In: *Batteries* 9.9 (2023). ISSN: 2313-0105. URL: https://www.mdpi.com/2313-0105/9/9/478 (cit. on p. 55).

[26] Simone Pelloni. «MODELLAZIONE TERMICA DI BATTERIE AD ALTA TENSIONE CON TECNOLOGIA LI-ION PER VEICOLI IBRIDI». MA thesis. Bologna: ALMA MATER STUDIORUM, 2016-2017 (cit. on p. 56).

[27] Xiaogang Wu, Siyu Lv, and Jizhong Chen. «Determination of the Optimum Heat Transfer Coefficient and Temperature Rise Analysis for a Lithium-Ion Battery under the Conditions of Harbin City Bus Driving Cycles». In: *Energies* 10.11 (2017). ISSN: 1996-1073. DOI: 10.3390/en10111723. URL: https://www.mdpi.com/1996-1073/10/11/1723 (cit. on pp. 58, 76).

[28] Eric Wan and Ronell Merwe. «The Unscented Kalman Filter for Nonlinear Estimation». In: vol. 153-158. Feb. 2000, pp. 153–158. ISBN: 0-7803-5800-7. DOI: 10.1109/ASSPCC.2000.882463 (cit. on p. 65).

[29] Stefano Favelli. «Robust Localization for an Autonomous Racing Vehicle». MA thesis. Torino: Politecnico di Torino, 2022 (cit. on p. 66).

[30] Giulia Cilio. «Optimization of the control logic of a hybrid electric vehicle exploiting ADAS information». MA thesis. Torino: Politecnico di Torino, 2020-2021 (cit. on p. 69).

[31] *Generate Drive Cycles for Real Driving Emissions*. URL: https://it.mathworks.com/help/autoblks/ug/generate-drive-cycles-for-real-driving-emissions.html (cit. on p. 70).

[32] Greg Welch and Gary Bishop. «Welch & Bishop , An Introduction to the Kalman Filter 2 1 The Discrete Kalman Filter In 1960». In: 1994. URL: https://api.semanticscholar.org/CorpusID:9209711 (cit. on p. 93).

[33] Liu hengrui Han zhuoyang. «Battery state of health and state of charge estimation with related application». MA thesis. Torino: Politecnico di Torino (cit. on p. 95).

[34] Saulius Pakstys. «Modelling,Control and Testing methodology of hybrid powertrains with recycled permanent magnet-based electric machines». MA thesis. Torino: Politecnico di Torino, 2023.

[35] *What is the difference between micro, mild, full and plug-in hybrid electric vehicles*. URL: https://x-engineer.org/micro-mild-full-hybrid-electric-vehicle/.

[36] Zul Hilmi Che Daud, Daniela Chrenko, Fabien Dos Santos, El-Hassane Aglzim, Alan Keromnes, and Luis Le Moyne. «3D electro-thermal modelling and experimental validation of lithium polymer-based batteries for automotive applications». In: *International Journal of Energy Research* 40.8 (2016), pp. 1144–1154. DOI: https://doi.org/10.1002/er.3524. eprint: https://onlinelibrary.wiley.com/doi/pdf/10.1002/er.3524. URL: https://onlinelibrary.wiley.com/doi/abs/10.1002/er.3524.

[37] mathworks. «MATLAB library». In: (). URL: https://it.mathworks.com/.